UCLouvain

AGRO LOUVAIN

Faculté des bioingénieurs

Multi-scale Classification of Photogrammetric Point Cloud Data

Towards Establishing a Digital Twin in Louvain-la-Neuve

Author:	Sinoj KOKULASINGAM
Supervisors:	**Prof. Pierre DEFOURNY** (UCLouvain | Earth and Life Institute – Environmental Sciences)
	Dr. Merle MURU (University of Tartu | Institute of Ecology and Earth Science – Department of Geography)
Jurors:	**Dr. Julien RADOUX** (UCLouvain | Earth and Life Institute – Environmental Sciences)
	Prof. Emmanuel HANERT (UCLouvain | Earth and Life Institute – Environmental Sciences)

Academic year: 2023 – 2024

Submitted in partial fulfillment of the requirements for the degree of:
Master [120] in agricultural sciences and bio-industries, with a professional focus: GEM – Geo-Information Science and Earth Observation for Environmental Modeling and Management (SAIV2MS/GM)

Acknowledgements

First and foremost, I would like to thank the GEM partners and associates for funding this amazing academic journey. Prof. Andy, you have realized my dreams of pursuing a career in geo-informatics. Laura, thank you for making my transition into the program seamless.

I owe an immense debt of gratitude to my thesis supervisors, Prof. Pierre Defourny and Dr. Merle Muru, who have both supported and contributed immensely to bring this project into fruition. I deeply appreciate your valuable notes and unwavering guidance in shaping this body of work. I would also like to extend my thanks to Dr. Julien Radoux for taking the time to provide me with incredibly helpful technical advice. In addition, I would like to thank the jury members, Dr. Julien Radoux and Prof. Emmanuel Hanert for taking the time to lend their scientific eye and evaluating the quality and rigor of my work.

I am deeply grateful for the love, and support that I have received throughout this journey from my colleagues, friends, and loved ones. Finally, a deep gratitude to my computer for not crashing during those crucial moments.

To my family, I love you.

Abstract

Under the context of establishing a digital twin, the first step after data collection is to extract meaningful information from dense big data. This work provides a starting point by semantically labelling a photogrammetric point cloud dataset and seeks to find the optimal descriptors for extracting building information in a study area within Louvain-la-Neuve. A multi-scale point-wise classification approach was adopted where the point cloud was iteratively subsampled three times at three progressively larger grid sizes. At each subsample, 15 feature descriptors derived from height, reflectance, and eigenvalue-based geometry were computed using exclusively free and open-source software. The model with all features combined performed the best achieving an overall accuracy of 0.94, though with major confusion between roof and ground points. Although, geometric features performed the worst reaching a low of 0.59 overall accuracy, it was proven that the combination of geometric features with other color or height information led to more accurate classification of roofs and facades. Moreover, the reflectance information from photogrammetry proved to be highly valuable for vegetation extraction. In order to evade the confusion between roof and ground, the ground points were segmented using Cloth Simulation Filter (CSF) followed by the reconstruction of a gapless DEM. This approach showed great potential as since it enhanced the classification accuracy reaching 95% overall accuracy without the introduction of external datasets. However, further validation of roof points with a rooftop dataset from the Wallonian cartographic dataset (PICC) showed that a quarter of points classified as roof were needed to be removed to attain a 91% validation accuracy.

Key words: multi-scale classification, semantic labeling, building extraction, photogrammetry, point cloud processing, geometric features, city 3D model

Table of Contents

List of Figures

List of Tables

List of Equations

List of Acronyms

ALL_FEAT	All Features Combined, with Absolute Height
ASPRS	American Society for Photogrammetry and Remote Sensing
CANUPO	*Caractérisation de Nuages de Points*
CFD	Computation Fluid Dynamics
CityGML	Geography Markup Language for City 3D Models
COL_HEI	Color and Absolute Height Only
COL_ONLY	Color Only
CSF	Cloth Simulation Filter
DEM	Digital Elevation Model
DSLR	Digital Single-Lens Reflex Camera
DSM	Digital Surface Model
DTM	Digital Terrain Model
FLANN	Fast Library for Approximate Nearest Neighbor
GCP	Ground Control Points
GEO_COL	Geometric Features with Color
GEO_HEI	Geometric Features with Absolute Height Features
GEO_ONLY	Geometric Features Only
GSD	Ground Sampling Distance
HEI_ONLY	Absolute Height Only
HSV	Hue, Saturation, Value Color Space
KNN	K-Nearest Neighbors
LAS	Laser File Format
LiDAR	Light Detection and Ranging
NO_GROUND	All Features Combined, With Relative Height
PDAL	Point Data Abstraction Library
PICC	*Projet Informatique De Cartographie Continue*
RF	Random Forest
RGB	Red, Green, Blue Color Space
SDGs	Sustainable Development Goals
SLURM	Simple Linux Utility for Resource Management
SPW	*Service Public de Wallonie*
sUAV	small Unmanned Aerial Vehicle
TLS	Terrestrial Laser Scan

Chapter 1. Introduction

Urban areas have been experiencing enormous population growth rates in the past years (UN DESA, 2022). Urbanization provides a higher number of job opportunities, better infrastructure, and advanced education (Bera et al., 2023). As a positive feedback loop, due to the high influx of people to cities, cities experience economic development and in turn, improved transportation services, increased exposure to cultural diversity and increase in services and facilities. They cater to the ever-increasing population, making the city more attractive (James et al., 1998). As a negative feedback loop, over population could overwhelm the previously mentioned services and facilities (Cho & Kim, 1983).

Urban expansion has led to rise in energy demands (Madlener & Sunak, 2011), high volume of traffic (Rao et al., 2021), lower agriculture productivity (Follmann et al., 2021). Moreover, environmental issues are exacerbated with more residents. Urbanization increases air and noise pollution (Sarzynski, 2012; Tong & Kang, 2021), induces flash flooding (Ajjur & Al-Ghamdi, 2022; Al-Ghamdi et al., 2012), reduces biodiversity (Sushinsky et al., 2013), changes hydrologic and biogeochemical cycles (Bera et al., 2023).

Global frameworks such as the Sustainable Development Goals (SDGs) encourage planners on developing strategies to nurture a sustainably conscious community with their city residents (Pradhan et al., 2017). Around 65% of the 169 targets associated with the 17 SDGs necessitate the involvement of local and regional city governments (Lafortune et al., 2019). The added pressure on cities have yet to produce fruitful results, since they are continuing to function under a business-as-usual approach (Liu et al., 2023).

The multi-faceted problem of cities could not be solved with a single solution. The sheer number of intertwining variables and different possibilities are too complex for humans to begin comprehending (Batty, 2014; Colding et al., 2020). Fortunately, computational power has increased exponentially and could incite a data-driven approach for designing, monitoring, and managing full-scale cities (Islam & Reza, 2019). The digitization of a city with its delicate web of networks is called a digital twin and has emerged as a prominent topic over the last 20 years (Deng et al., 2021). A rising number of countries regard the integration of the physical world with the virtual world as a solution to the environmental and logistical issues of a metropolis (Azevedo Guedes et al., 2018).

Digital twins enable planners and managers with (near) real-time monitoring data, energy optimization tactics, automated traffic flow and public transit management, water resource management, moreover, they can assist in resource allocation and disaster risk management (Deng et al., 2021; Yin et al., 2015). Nevertheless, to achieve the futuristic scenario, where

computer models could facilitate urban planning and management, several key challenges need to be addressed, such as finding an efficient way for the integration of data systems from a wide array of sensors and other data sources. Additionally, a continuous monitoring of the city and the different parameters needed to maintain sustainable development could be challenging.
The first challenge of establishing a digital twin is the acquisition of data for creating the city in virtual format. The advent of low-cost acquisition methods, such as laser scanning and digital photogrammetry has opened the doors for rapid and easy data collection (Pérez et al., 2013). However, the data collected is considered big data, due to the sheer volume of information acquired to represent the complexities of the physical world (Isa et al., 2018). As this data is impractical without the means to extract meaningful information, the field of computer vision and 3D scene processing has become highly popular with 3D data processing applications (Weinmann et al., 2013). Among algorithms that segment and extract information based on clustering similar features, the semantic classification of 3D data is a constantly evolving topic (Becker et al., 2018; Thomas et al., 2018). Many applications such as flood modelling, solar potential calculation, noise mapping require classified 3D city models for further complex analyses (Biljecki et al., 2015).
Therefore, this study will aim to adopt a classification methodology capable of classifying an urban setting and find the information that works best for isolating building structures such as facades and rooftops.

This work begins with a literature review providing background information about the role of city 3D models and their potential. The first step of creating a 3D model is acquiring data and processing it to obtain semantic information, therefore, both topics are explored in detail. Then, the objectives and research questions are stated. The datasets and methodology used in this study are given a comprehensive explanation, followed by an analysis of the results obtained by the classification model and its performance. The discussion chapter provides the interpretation of the results highlighting the different implications of the analyzed data and whether they conform to the state-of-art. The chapter ends by stating the limitations of the model and provides several recommendations for future research avenues. Finally, the work is summed up succinctly with closing remarks.

Chapter 2. Literature Review

This chapter presents a literature review on the applications of 3D city models and the pre-processing needed to distinguish one structure in the point cloud from another. It aims to highlight the important role 3D city models have been playing in the scientific landscape, in addition to the state-of-the-art techniques in extracting meaningful information for the semantic classification of point clouds for creating 3D city models.

2.1. The role of city 3D models

A 3D city model encompasses the digital representation of the city's physical structures and is used to realize a smart society.

The growing interest in smart cities could be attributed to the need to increase efficiency and enhancement of city services and infrastructure (Azevedo Guedes et al., 2018); to provide climatic simulations and pollution predictions (Bekkar et al., 2021); to calculate renewable energy potential in an urban landscape (Romero Rodríguez et al., 2017), among other applications in urban planning (Chen, 2011). While 3D city models are one of the primary precursors for establishing a digital twin, some shortcomings need to be addressed to acquire the closest possible results to the real physical world.

Building simulation models require large amounts of data, which could not be the case for every city. Furthermore, data validation for big data poses another layer of complication (Strzalka et al., 2011).

3D city models for the same region could have substantial differences due to different acquisition methodologies, reconstruction from raw data, and processing algorithms. These differences can create multiple inconsistencies between models, which impede data interoperability and their use in certain applications (Stoter et al., 2020). Moreover, Stoter et al. (2020) mention that standardization of city 3D models is imperative for consistent formats and data structuring to preserve geometry and the semantic information of each building, such as year of construction, building material, number of floors, and number of inhabitants. By digitizing each building within the urban landscape, a vast array of potential use cases is unlocked, benefitting each city resident.

2.2. Use cases of 3D city models

2.2.1. Hazard Risk Management

Urbanized areas currently house more than half the human population (UN DESA, 2022). Therefore, city 3D models could be used as a tool in the decision-making process of hazard risk

prevention and management. Computational fluid dynamics (CFD), within a city context, seeks to tackle issues such as air pollution monitoring, wind movement analysis and flooding events (Ridzuan et al., 2022). Ujang (2015) argues that the potential for using virtual city models is immense for air quality simulation since the usage of air quality monitoring stations is inconsistent and impractical in cities due to their complex configuration. Ridzuan et al. (2023) focused on simulating wind flows with cityGML data using the Realizable K-epsilon (k-ε) turbulence model. The cityGML third level of detail was chosen since it contains the bare minimum features required for modeling wind flow estimation and visualization. The simulation model outputs the interaction of wind with the city models and insights into the pressure, kinetic energy, turbulence, and rate of dissipation. Schröter et al. (2018) demonstrated the potential of city 3D models and their capacity to enable urban planner with informed decisions about managing flood scenarios and identifying high risk areas. They predicted damages to buildings, inundation depth and economic losses in the event of a flood using flood loss models on 3D city model. Furthermore, Willenborg et al. (2018) showed that CFD can simulate catastrophic events such as individual blast scenarios. The simulation engine they used was able to return a collection of probabilities for the material and bodily damage incurred. Specifically, they were able to pinpoint the specific glass facades within the study area that had more than a 70% probability of shattering.

2.2.2. Energy demand estimation

City 3D data provides volumetric information about the urban landscape alongside semantic information such as building typology, number of floors and year of construction. In this use case, 3D city modelling can be a highly beneficial for decision-makers as it facilitates diagnostics of the existing building stock and enabling the adoption of sustainable energy strategies. Such data can be utilized to model and estimate the energy demands of individual buildings (Biljecki et al., 2015; Nouvel et al., 2013; Willenborg et al., 2018) to minimize greenhouse gas emissions. Strzalka et al. (2011) predicted the heating energy demand of Scharnhauser Park in Ostfildern, Germany. They used hourly air temperature, orientation of windows, global radiation data, and heat transfer coefficient data for the simulation model. A city model of Berlin was also utilized to estimate the entirety of the German capital's net energy demand by deriving building geometry information such as thematic hull surfaces, building volumes, and floor heights from the semantically labeled 3D model (Kaden & Kolbe, 2013). The potential of simulating energy demands, more specifically, predicting heating demands at the level of individual buildings, were explored by using a country-wide 3D city model of the

Netherlands (León-Sánchez et al., 2021). Similarly, Murshed et al. (2018) utilized the advantage of 3D city models' building attributes to model building heating and cooling energy needs on monthly basis on multiple cities across Asia and Europe.

2.2.3. Noise mapping

Noise pollution can be visualized by 3D models, where the noise generated by oncoming traffic can be mapped onto the city model. Such visualizations could give insight into several mitigation measures, in addition, the third dimension provides a clearer image of the effect of refraction and diffraction due to barriers and the degree of sound attenuation with altitude (Biljecki et al., 2015; Zhao et al., 2016). GIS and 3D models could be integrated for noise modelling and ease of dissemination through the internet for visualization (Kurakula et al., 2007). Stoter et al. (2008) simulated noise pollution in an urban environment using interpolation techniques and compared the differences between 2D and 3D analysis of noise pollution. They found that the number of populations affected by noise was highly underestimated in the 2D analysis. Likewise, Lu et al. (2017) modeled sound propagation paths to pinpoint the degree to which different sound sources, such as road, railway or traffic posed an annoyance to observer points on building facades. Their result displayed the location of buildings most to least affected by high incoming noise from the transportation sector.

2.2.4. Renewable resource calculation

The three-dimensional aspect of city models have been used extensively for solar potential estimation. When compared with 2D models, the solar irradiance estimates used with 3D models resulted in a more accurate output, though, complex architecture needed higher definition models (Kolečanský et al., 2021). Bremer et al. (2016) utilized topographic data and city 3D models to determine irradiation values in the Old Town of Innsbruck, Austria. The daily irradiation was simulated using a ray-tracing procedure that considers the rooftop and facades of the city in relation to the sun's azimuth and inclination. The result was visualized on the city model as a texture map, where they had concluded that the daily irradiation was more homogeneous on rooftops than that of the facades. In addition, they had derived that the city receives an average of around 340 kWh per half year for all surfaces. Certain acquisition techniques such as LiDAR provides information about nearby obstructions, rooftop orientation and slope information, which could be used alongside climatic and temporal data to discern neighborhoods with higher solar potential (Suomalainen et al., 2017). Huang et al. (2015) developed an augmented model capable of estimating direct and indirect roof solar energy

potential by inputting LiDAR data to attain high resolution information about complex urban environment. The model also takes into account the atmospheric clearness index, making it more robust at estimating solar potential during cloudy settings. Chen et al. (2022) developed the model further by computing solar potential using a grid-based schema and used airborne photogrammetry for the extraction of rooftops. Waqas et al. (2023) used LiDAR and 3D building data of Texas, USA to extract sun and sky maps and pinpoint areas of high suitability for photovoltaic placements by implementing a viewshed algorithm.

2.3. The creation of 3D city models from point clouds

2.3.1. Data acquisition

Remote sensing has become increasingly vital for acquiring structural features and topographic data in three-dimensional space. Features such as vegetation, buildings, vehicles, and ground surfaces can be used to establish a digital twin of the surveyed area (Schrotter & Hürzeler, 2020; Verma et al., 2006; Xue et al., 2020).

An urban area could be captured as a 3D representation using light detection and ranging (LiDAR) techniques such as airborne laser scanning, where an airborne sensor actively emits light pulses and receives back the height information. The time elapsed for the light pulse to travel back and forth provides information regarding the distance (Collis, 1970). The resulting data could be utilized to analyze the topography of the study area in the form of a digital surface model (DSM) and digital terrain model (DTM). Another form of LiDAR, terrestrial laser scanners (TLS) could also collect three-dimensional information about cities from lower point of views. TLS is an automated total station that could be equipped with a camera to acquire both reflectance and 3D point data (Bornaz et al., 2004; Feng & Guo, 2021).

An alternative technique is photogrammetry, which is an airborne or terrestrial imaging technique that involves overlapping consecutive images (Sahin et al., 2012). These images are used to create an orthorectified mosaic image of the surveyed plot. The apparent displacement of the same object from one image to another is termed parallax (Schenk, 2005). Parallax enables the extraction of height information and, in turn, reconstruct 3D objects through techniques such as structure from motion (Schenk, 2005; Westoby et al., 2012).

Nonetheless, a digital model can also be produced from 2D data that would be extruded in the third dimension according to the given height information (Biljecki et al., 2015). A sparsely spaced point cloud reconstruction of an urban environment can also be performed by using publicly available Google Street View Images (Cavallo, 2015).

Both surveying techniques, LiDAR and photogrammetry, lead to the representation of the actual world digitally in three-dimensional coordinates (X, Y, and Z). Moreover, the points also provide additional information that is unique to each technique. For example, LiDAR data measures the return strength or intensity, which is useful for identifying and classifying features. On the other hand, photogrammetry relies on photographic images and provides radiometric information. While both techniques are used to produce 3D models of landscapes, LiDAR products retain higher precision and accuracy since unlike photogrammetry, where the image quality relies on the camera used and the mosaic needs to be geo-referenced, LiDAR point clouds are already geo-referenced since the sensor is equipped with high-precision GNSS sensors (Baltsavias, 1999). Furthermore, due to the need for ground control points (GCP) laid throughout the survey area with accurate measurements of their respective coordinates for photogrammetry, LiDAR is a better alternative for inaccessible areas. However, with the advent of low-cost commercial small unmanned aerial vehicles (sUAV), high-resolution cameras, and widely accessible post-processing tools, the popularity of photogrammetry has increased over the last decades to survey ground topography and features (Pérez et al., 2013).

The reconstruction of digital elevation models, generation of orthophotos, and point clouds attained through algorithms such as structure from motion (SfM) (Westoby et al., 2012) can be used for various array of applications such as precision agriculture (Tsouros et al., 2019), mapping mine areas (Xiangfeng Liu et al., 2012), detecting forest disturbance dynamics (Minařík & Langhammer, 2016), and archaeological surveys (Saleri et al., 2013).

Though, raw photogrammetric point clouds lack information on surface reflectivity and do not differentiate semantically between points, one of the primary advantages of using photogrammetry point records as opposed to LiDAR-based data is the benefit of having color information derived from the set of images.

Popular image-based modeling software, such as Agisoft Metashape is a closed-source software that possesses user-friendly tools for point cloud classification (Agisoft, 2024). Its ease of use and direct workflow have led to its widespread use for the reconstruction of digital terrain models and point filtering. However, the final output lacks the accuracy achieved by a more technical pipeline (Howland et al., 2022). Pix4D is a market leader in processing UAV images and photogrammetry (Pix4D, 2024). Pix4D is commercial software, that is capable of producing point clouds of comparable accuracies to Agisoft in relatively noncomplex study areas (Alidoost & Arefi, 2017), while performing better in dense urban areas (Shoab et al., 2022). Pix4D possesses both supervised and unsupervised classification tools, where it uses a preset of classes to segment the point cloud according to geometry and color information.

However, Ntuli & Forbes (2023) showed that its classification performance is not robust to isolate buildings with predominant type I errors, i.e. several cases of false positive classification.

On the other hand, CloudCompare (Girardeau-Montaut, 2014) is a free and open-source 3D point cloud visualization and processing software. It has supervised classification features such as the *Caractérisation de Nuages de Points* plugin (CANUPO) developed by Brodu & Lague (2012). However, in practice, CANUPO is limited in functionality as it is a binary classifier but provides satisfactory classification results (Ntuli & Forbes, 2023).

2.3.2. Segmentation

A technical workflow for point filtration derived from aerial photogrammetry depends on the application in question. One of the first necessary steps for post-processing raw photogrammetric point clouds is segmentation and semantic classification of each point to isolate relevant features pertaining to the research objective. Segmentation refers to grouping points with similar geometric or radiometric properties, whereas classification assigns semantic labels to each point (Grilli et al., 2017).

As a preliminary step without prior classification, segmentation of the point cloud can lend insight into how the points are arranged in space based on each point's neighbors. Rabbani et al. (2006) utilized surface normal vectors to assess the local connectivity of the points, thus segmenting their data according to surface smoothness, i.e., the collection of points that have a low variation in the surface normal vectors. Edge-based segmentation is another technique that extracts the contours of features and segments the points within and outside of the boundaries (Wani & Arabnia, 2003). In order to segment ground points, Zhang et al. (2016) proposed a novel approach, the cloth simulation filter (CSF), where the point cloud is turned upside down and a rigid cloth grid made of interconnected particles is simulated to cover the inverted surface. After a few iterations and post-processing steps, the cloth takes the form of the terrain's topography, thus effectively segmenting ground, and non-ground points.

2.3.3. Geometry features

Weinmann et al. (2013) developed a point-based segmentation methodology, where each point's neighborhood provides a mathematical relationship between the point and its orientation in three-dimensional space. Point-based segmentation relies on the calculation of geometric features derived from the covariance matrix of the point itself and its neighbors. The neighborhood could be selected according to a fixed number of surrounding points (K-Nearest

Neighbors), a spherical neighborhood, or a cylindrical neighborhood around every point (Weinmann et al., 2015a). While cylindrical neighborhoods are more often used in LiDAR data, K-Nearest Neighbors (KNN) and spherical neighborhoods are more popular with airborne photogrammetric data (Niemeyer et al., 2014; Thomas et al., 2018).

Following the selection of a neighborhood, the three-dimensional structure and orientation of the local neighborhood can be broken down by the eigenvalue-based geometric features (Weinmann et al., 2013). Eigenvalue-based geometric features describe each point's spatial arrangement and explain their structural composition within the point cloud. They provide robust attributes for distinguishing objects due to the invariant nature of eigenvalues in rotation, translation, and scaling. Moreover, eigenvalues are unaffected by non-uniform point clouds (Jutzi & Gross, 2009). Hence, they are well-suited for complex data sets, granted that the neighborhood adequately encompasses the details of the features (Jutzi & Gross, 2009; Thomas et al., 2018).

Succinctly, geometric features are a set of equations taking into account the eigenvalues at each axis and the eigenvectors. They describe the extent of each neighborhood's spatial distribution, orientation and randomness with respect to the point cloud (Weinmann et al., 2013).

Omnivariance is defined as the determinant of the covariance matrix. It emphasizes the volumetric spread of the points within the neighborhood, i.e., it measures the degree of isotropy within the neighborhood. Therefore, it leads to the discrimination between points that are spread out heterogeneously along the three-dimensional space, such as vegetation, and homogenous collections of points such as facades and ground (Günen, 2022).

Eigenentropy relates to the measure of the order of disorder of the neighborhood derived from the covariance matrix and could mainly isolate corners, edges, and surfaces (Günen, 2022; Weinmann et al., 2013).

Anisotropy is the ratio between the smallest eigenvalues and the largest eigenvalues and represents the directional dependency of a structure. Hence, it is useful in discriminating between linear and volumetric objects (Thomas et al., 2018).

Linearity measures the degree to which points form a linear structure. Linearity is important for highlighting elongated objects such as buildings corners or lamp posts, while planarity measures the degree to which the points in the neighborhood fit on a flat plane. A deviation from the flat plane could be measured by using curvature as a geometric feature (Weinmann et al., 2013).

Verticality captures how upright the neighborhood is in relation to the Z axis. It is a measured by calculating either the deviation of the eigenvectors of the neighborhood from the normal

vector Z (Hackel et al., 2016) or by calculating the angle between the first and last eigenvectors (Thomas et al., 2018).

Hackel et al. (2016) extended on the set of equations by adding the calculation of height values such as the range of height within the neighborhood and the height above and below the neighborhood's center. Becker et al. (2018) further advanced this approach by incorporating reflectance information, which notably enhanced the semantic classification of points. Instead of using the red, green, and blue (RGB) bands, they converted the values into the hue, saturation, and value (HSV) domain. This conversion was conducted since their training data showed higher information gain in the HSV domain according to Pearson product-moment correlation coefficient analysis.

2.3.4. Multiscale neighborhoods

The inclusion of multiple scales for the neighborhood could improve classification. Multiple scales are an important addition to consider since a surveyed area contains features of varying sizes (Thomas et al., 2018) and is capable of revealing different properties of the underlying surface (Hackel et al., 2016). However, iterating through a large point cloud dataset, which could potentially contain points in the order of millions, and performing matrix calculations for each point's neighborhood is a resource-intensive task (Arya et al., 1998) even when a hierarchical K-Dimensional searching algorithm such as a KD-tree is utilized (Friedman et al., 1977).

Consequently, rather than searching for the exact neighboring points, approximations of the neighborhood could reduce computation times significantly with limited loss in accuracy (Weinmann et al., 2015a). Hackel et al. (2016) had provided an optimized solution for approximating neighborhoods. They proposed the iterative subsampling of the entire point cloud into decreasingly less dense multi-scale pyramids. Followed by calculating the geometric features at proportionally smaller search structures at each scale. Such a methodology would disregard the need to find the optimum scale at which to compute the features (Atik et al., 2021; Weinmann et al., 2013) and could systematically cover all appropriate scale levels. Subsampling of the point cloud refers to the reduction of the point density of the existing point cloud while maintaining the detailed characteristics of objects. It could be carried out by dividing the data into voxel grids and retaining only the centroid of each voxel (Hackel et al., 2016; Thomas et al., 2018), partitioning the point cloud into octrees (El-Sayed et al., 2018; Zheng et al., 2024), or reducing the point density using spatial correlation between the ground coordinates and the center of the pixel (Huang et al., 2020).

Efficient neighborhood retrieval includes calculating the K-Nearest or spherical neighborhoods with optimizing libraries such as the Fast Library for Approximate Nearest Neighbor or FLANN (Muja & Lowe, 2009), which is an efficient library for finding the optimum algorithm to retrieve the neighbor matrix (Thomas et al., 2018; Weinmann et al., 2015b). Adapting the iterative subsampling method proposed by Hackel et al. (2016), Thomas et al. (2018) incorporated multi-scale spherical neighborhoods coupled with a density parameter for the neighborhood query instead of KNN and achieved a classification algorithm comparable to more sophisticated methods including convoluted neural networks.

2.3.5. Semantic labeling

Once the geometric features are extracted for the point cloud, the assigning of labels to each point could be done using machine-learning or deep-learning approaches.

Using the supervised machine learning approach, reference data containing training samples for each label category is prepared. It is, then, used to train off-the-shelf machine learning classifiers for the semantic classification of the full dataset. Publicly available laser scan or point cloud datasets have been used to benchmark different methodologies and workflows.

Atik et al. (2021) used 8 different machine-learning classifiers to classify datasets at 5 different scales individually. They found that the highest overall accuracy of 93% was achieved with a spherical neighborhood of 3 meters and with a Random Forest (RF) classifier. Similarly, Becker et al. (2018) incorporated color information and geometric features. They found that RF and Gradient-Boosted trees performed significantly better with color information with low overall errors. Thomas et al. (2018) compared the performance of RF performance in classifying indoor and outdoor point clouds with deep learning algorithms. They concluded that multiscale features coupled with RF classification ranked among the best classification techniques, outdoing most elaborate algorithms.

The applications of 3D cities and their eventual development into a digital twin is a key solution for decision-makers. Enabling them to address critical issues that threaten urbanized areas such as natural disasters, population increase, traffic management and energy demand optimization with data-driven solutions. At this stage, it is a fast-paced field of research with lack of a standardized workflow for data acquisition, processing and creating a city 3D model.

Thus, this study aims to provide the first step of a comprehensive workflow under the framework of establishing a digital twin. One of the key steps for creating a digital twin is having a city 3D model that is semantically labelled to isolate different structures easily for more complex applications.

Chapter 3. Research objectives

The study pioneers the development of a digital twin task by classifying a photogrammetric point cloud into several semantic labels in an accurate manner. Moreover, the study tests the classification model on a point cloud dataset that was obtained through a cutting-edge data acquisition method over the Belgian city of Louvain-la-Neuve.

The city is within the region of Wallonia and is located 30 km southeast of the Belgian capital, Brussels. The pedestrian-centric 15-minute city is mostly constructed on a raised platform, having the main road and railway pass underneath rather than through it (Charlier, 1977). Thus, most of the city is characterized with a high degree of urbanized architecture. The tile used for testing the classification model in this study is situated 500 meters southeast of the city center in Croix du Sud. The extent is mostly dominated by large academic buildings in the center and smaller residential buildings on the borders. The buildings are interspersed with urban street trees, several public parks in addition to the two-lane Boulevard Baudouin 1er crossing almost diagonally. Subsets for reference data were chosen at random. They are spaced evenly throughout the study area to encompass different morphologies and features.

A special emphasis was made in this study to exclusively use free open-source software for the analysis of point cloud data and the generation of cartographic products. Thus, the methodology of this study was not based on closed-source computer code and could be replicated by anyone. Software such as CloudCompare and QGIS were used for visual analysis, while Python packages such as laspy, numpy and rasterio were considered for mathematical calculations.

The objectives of this study could be summarized into the following research questions:

1. How varying is the accuracy of multi-scale classification of the point cloud dataset of Louvain-la-Neuve compared to literature?
2. Within the context of the study area and type of data used, do geometric features enhance the classification in the study area?
3. Which classification features best describe building facades and roofs in the study area?
4. Would subsampling the point cloud lead to the loss of data?

Chapter 4. Materials and Methods

Establishing a 3D model for Louvain-la-Neuve from photogrammetric data relies on a classified point cloud, which distinguishes between ground and non-ground elements such as vegetation, vehicles, and buildings. Therefore, a supervised classification was needed for the semantic labelling of the point cloud. The resulting points could be later used for creating a digital elevation model, isolation of vegetation, and creating 3D building models with a higher level of detail than extruding to rooftop points. The classification procedure of this study is characterized by the following workflow: (1) establishing a reference point cloud through manual classification, (2) subsampling both the reference and the study area point cloud, (3) extracting descriptive features from height, reflectance, and geometric information, (4) classify the point cloud using the RF machine learning algorithm, (5) validate and check the output for misclassifications.

4.1. Point cloud data

Aerial photogrammetric images were acquired by the Belgian aviation company Sourse (formerly known as Stratos Solution) under the order of UCLouvain-Geomatics lab.

The pioneering survey took advantage of recent technology by means of rapid deployment technology operating at a relatively low cost. The survey over Louvain-la-Neuve took place at an altitude of 636 meters (above ground level) travelling at a cutting-edge speed of 90 knots (ca. 167 km/h) at multiple angles. The fly-over was conducted using a fixed-wing aircraft equipped with two Canon EOS 5DS R DSLR cameras and a Phase One iXM-RS150F camera dedicated to aerial photogrammetric applications. Both camera models have ultra-high resolution with a 4.24 and 3.76 μm pixel size, respectively. The resulting point cloud used in this study was provided by Sourse and UCLouvain. The dataset had a ground sampling distance (GSD) of 3.36 cm/pixel. Each point record contains three-dimensional position (encoded as X, Y, and Z coordinates encoded in the Belgian Lambert 72 coordinate system) and reflectance information (encoded with red, green, and blue bands). The data was provided as an uncompressed LAS file covering multiple tiles for the whole city. Table 1 outlines the metadata of the Sourse photogrammetry mission.

Table 1. Details of the aerial survey

Date of acquisition	31/08/2022
Cameras	• 2 x Canon EOS 5DS R, EF85mm f/1.4L • Phase One iXM-RS150F equipped with Rodenstock RS 50mm-Ar lens
Pixel size	• 4.24 x 4.24 µm • 3.76 x 3.76 µm
Intra-band overlap	85%
Inter-band overlap	75%
Ground sampling distance	3.36 cm/pixel
Aircraft type	Sonaca S201 Surveyor
Flight speed	167 km/h
Altitude	636 meters

A single tile of the study area, spanning 249,983 square meters, was extracted from this dataset to ensure the working of the classification model with reasonable processing times. The tile was checked to have a sufficient representation of the buildings and vegetation of Louvain-la-Neuve (Figure 1). Furthermore, the study area tile was made up of 141,082,464 points, thus having a point density of 564.37 points/m^2.

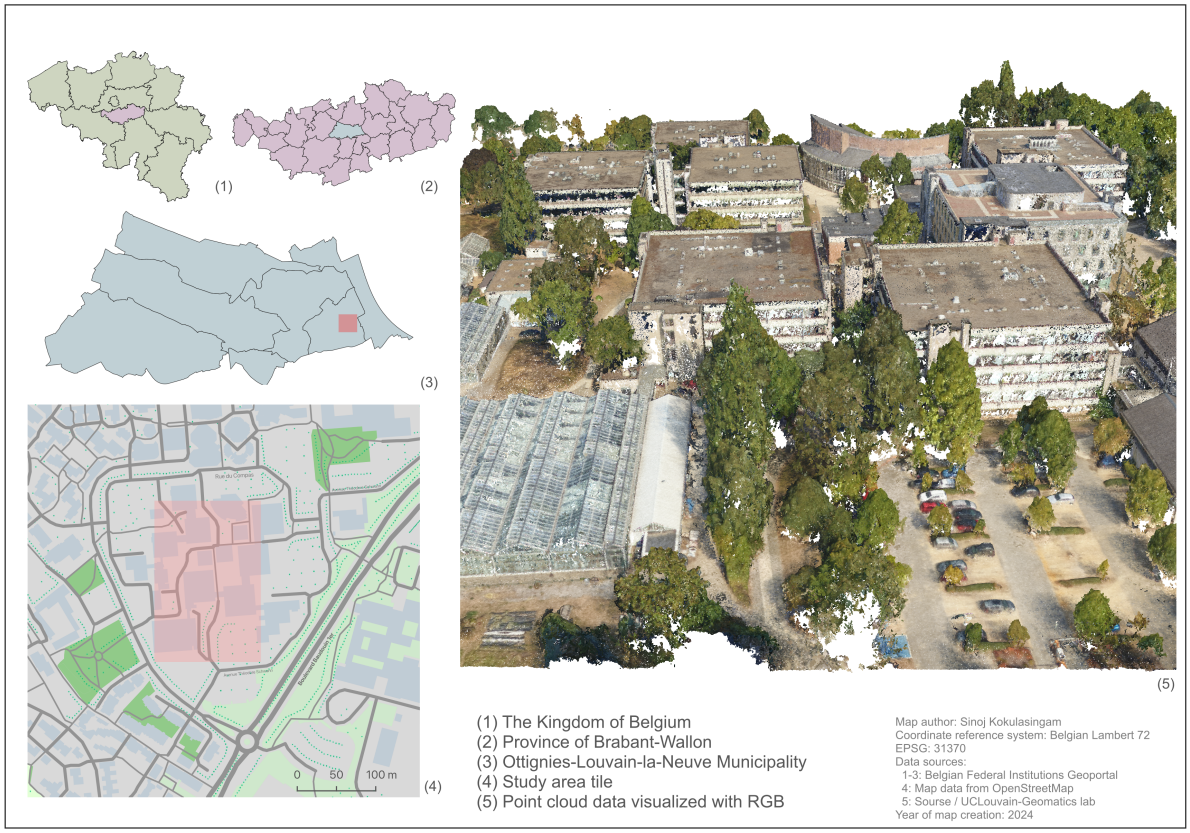

Figure 1. Map showing the study area tile's location within Belgium (left) and a bird's eye view of Croix du Sud.

4.2. Reference point cloud

Representative subsets of the study area tile were randomly chosen and manually classified to be used as reference data for training the RF classifier. The reference point cloud covered an area of 47,970 square meters and contained 28,910,465 points. By visually interpreting, seven classes were identified as necessary to describe the scene: ground, building rooftops, building facades, and vehicles. Although the study's main focus is to extract building structures, the vegetation within the study area was also given attention in order to be comparable with previous publications (Becker et al., 2018; Thomas et al., 2018; Weinmann et al., 2013). Thus, three vegetation sub classes based on height were established: low, medium, and high (Figure 2). In this study, the low vegetation label was reserved for short ornamental shrubs and bushes found within parking lots and in-between houses. The medium vegetation label referred to points interpreted as trees having an elevation roughly between 130 and 170 meters (above sea level), while the taller poplar and coniferous trees were labeled as high vegetation.

In order to adhere to the naming and labeling convention, classification values and semantic labels were taken from the American Society for Photogrammetry and Remote Sensing (ASPRS) standards and specifications (Graham, 2015) (Table 2). The cloth-simulation filter

algorithm was utilized in order to facilitate the laborious task of manual classification (Zhang et al., 2016). Although imperfect, the filter distinguished a majority of the ground points from others. The removal of ground points facilitated the isolation of points representing vegetation, vehicles, and buildings. CloudCompare version 2.13 was used to select and label the points in the reference point cloud manually.

Table 2. Typology providing semantic labels and related classification values to establish the reference point cloud. The share of each label from the total points (28,910,465) is also presented.

Classification label	Classification value	Number of points labelled	Proportion of each class (%)
Ground	2	5,458,881	18.88
Low Vegetation	3	1,514,211	5.24
Medium Vegetation	4	9,819,623	33.97
High Vegetation	5	323,654	1.12
Roof	6	5,096,101	17.63
Facade	7	6,449,021	22.31
Vehicle	12	248,974	0.86

Therefore, the reference point cloud is a semantically classified point cloud containing office and residential buildings alongside parking lots and city trees. It was used for both algorithmically calculating descriptive features and training the RF classifier (Figure 2).

Figure 2. Map of the manually classified reference point cloud.

4.3. Feature extraction

4.3.1. Absolute height-based features

Height values are utilized for the clear distinction between features that might differ on the Z-axis but might not possess geometric variations, such as low, medium, and high vegetation. The z-coordinate value of each point record is used as a descriptor for RF. Moreover, as the model is already querying for each point's neighbors, descriptive height statistics of each neighborhood were computed to obtain holistic and robust discernment between features that have vertical height differences (Becker et al., 2018; Hackel et al., 2016).

4.3.2. Relative height-based features

The height of the points within the dataset in relation to the height of a reference plane (i.e., the study area's ground height) was derived by first separating the ground point's elevation, then, calculating the elevation difference between the rest of the points' elevation from the reference plane (Figure 3). The ground points were isolated by using CSF with a 0.2-meter cloth resolution, 500 iterations and a 0.5-meter classification threshold using CloudCompare (Zhang et al., 2016). The segmented ground points were then used to produce a DEM with a resolution

of 5 meters using the Point Data Abstraction Library (PDAL) (Butler et al., 2021). However, the resulting raster contained no data values at the locations of non-ground points. Consequently, QGIS's Fill NoData interpolation algorithm was applied in order to obtain a gapless DEM (QGIS developers, 2024). The DEM was used as input within the main workflow, where each point was iterated over after subsampling the point cloud. Relative heights were computed as the difference between each point's elevation and the value of the DEM at that point's location (Equation 1).

$$Z_{relative} = Z_p - Z_{DEM} \quad (1)$$

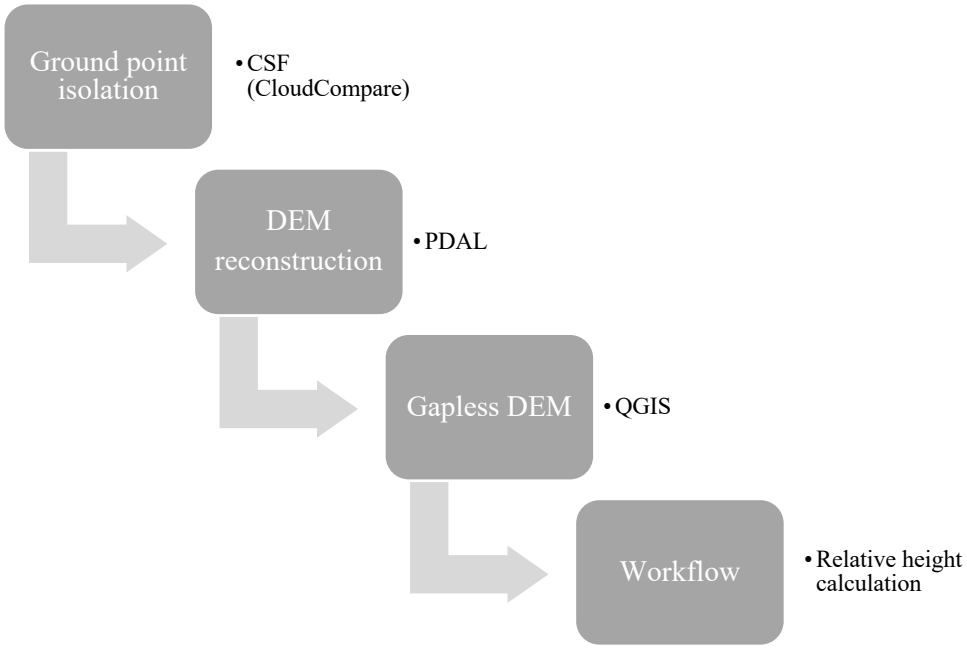

Figure 3. Overview of ground point extraction and their conversion to a DEM for relative height computation.

4.3.3. Color-based features

This study took advantage of the reflectance values for the three visible bands (i.e., color) red, green, and blue (RGB) for classification.

The reflectance bands are coded in 16 bits, ranging between a minimum value of 0 to a maximum value of 65,356 (2^{16}). Hence, the bands were first normalized to range between 0 and 1 by dividing original RGB values with the maximum value. Afterwards, similar to Becker et al. (2018), the discriminative power was enriched by converting the color data to the hue, saturation, and value (HSV) color space with Equations (2), (3), and (4).

$$Hue = \begin{cases} 0 & ,if\ \min(RGB) = \max(RGB) \\ 60 \times \dfrac{G-B}{\max(RGB)-\min(RGB)} & ,if\ R = \max(RGB) \\ 60 \times \dfrac{B-R}{\max(RGB)-\min(RGB)} + 120 & ,if\ G = \max(RGB) \\ 60 \times \dfrac{R-G}{\max(RGB)-\min(RGB)} + 240 & ,if\ B = \max(RGB) \end{cases} \quad (2)$$

$$Saturation = \begin{cases} 0 & ,if\ \max(RGB) = 0 \\ 1 - \dfrac{\min(RGB)}{\max(RGB)} & ,otherwise \end{cases} \quad (3)$$

$$Value = \max(\mathrm{RGB}) \quad (4)$$

Finally, not only were the color values of the individual points themselves used as attributes but the average color information of the whole neighborhood was also computed alongside the geometric features in order to obtain a robust classification.

4.3.4. Geometric features extraction

The two most widely used techniques for neighborhood selection are either extracting a fixed set of k-nearest points or selecting the nearest neighbors within a spherical volume for each point where the point itself is included in the neighborhood. In this study, the neighborhood query was done using a KD-tree, and a spherical neighborhood was chosen since it has been shown to outperform k-nearest neighbors (Thomas et al., 2018). For each neighborhood, if the number of points is fewer than 4, then a null value is assigned for all the eigenvalue-based geometric features. However, if more points were retrieved a meaningful covariance matrix C Equation (5), which represents the spread and orientation of the points around the centroid, was computed.

$$C = \begin{pmatrix} \sigma_{xx} & \sigma_{xy} & \sigma_{xz} \\ \sigma_{yx} & \sigma_{yy} & \sigma_{yz} \\ \sigma_{zx} & \sigma_{zy} & \sigma_{zz} \end{pmatrix} \quad (5)$$

Where Equation (5) encapsulates the variances between dimensions (σ_{xx}, σ_{yy}, and σ_{zz}) and the covariances between pairs of dimensions (σ_{xy}, σ_{xz}, σ_{yx}, σ_{yz}, σ_{zx}, and σ_{zy}). Equation (6) demonstrates the calculation of the covariance matrix within a neighborhood.

$$\sigma(N) = \frac{1}{N(r)} \sum_{p \in N(r)} (p - \bar{p})(p - \bar{p})^T \quad (6)$$

Where N represents the number of points in the neighborhood including the point itself, $\bar{p}$ denotes the medoid of the spherical neighborhood and T denotes the transpose operator. The covariance matrix is used to derive the eigenvalues λ_i and the eigenvectors $\overrightarrow{e_i}$ where $i = 1,2,3;\ \lambda_1 \geq \lambda_2 \geq \lambda_3$. Lastly, each eigenvalue was normalized by dividing the value with the total as shown in Equation (7).

$$\lambda_{normalized} = \frac{\lambda_i}{\sum_{i=1}^{3} \lambda_i} \quad (7)$$

4.3.5. Summary of feature descriptors

Ultimately, 15 features were used to describe the height, color, and geometric distribution of points, including features based on the eigenvalue's information. The feature vectors used in this study are listed in Table 3.

Table 3. Set of height, color, and geometric features used in this study, in addition to some of the literature in which the features have been used. Refer to section 2.3.3 for the explanation of the geometric features used in this study.

Derived from	Feature	Formula definition	Reference
Height	Height value	Z_p	(Atik et al., 2021; Hackel et al., 2016)
	Height mean	$\frac{1}{N(r)} \sum_{p \in N(r)} \mathrm{Z}$	(Atik et al., 2021; Hackel et al., 2016)
	Height above	$Z_{max} - Z_p$	(Hackel et al., 2016)
	Height below	$Z_p - Z_{min}$	(Hackel et al., 2016)
	Height range	$Z_{max} - Z_{min}$	(Hackel et al., 2016; Huang et al., 2020)
Color	Hue, Saturation, Value	$[H_p, S_p, V_p]$	(Becker et al., 2018; Thomas et al., 2018)
	Mean neighborhood color	$\frac{1}{N(r)} \sum_{p \in N(r)} [\mathrm{H}, \mathrm{S}, \mathrm{V}]_p$	(Becker et al., 2018; Thomas et al., 2018)
Geometric (Eigenvalues and eigenvectors)	Omnivariance	$\sqrt[3]{\prod_{i=1}^{3} \lambda_i}$	(Atik et al., 2021; Hackel et al., 2016; Thomas et al., 2018; Weinmann et al., 2013; West et al., 2004)
	Eigenentropy	$\sum_{i=1}^{3} \lambda_i ln \lambda_i$	(Atik et al., 2021; Hackel et al., 2016; Thomas et al., 2018; Weinmann et al., 2013; West et al., 2004)
	Anisotropy	$\frac{\lambda_1 - \lambda_3}{\lambda_1}$	(Atik et al., 2021; Hackel et al., 2016; Thomas et al., 2018; Weinmann et al., 2013; West et al., 2004)
	Linearity	$\frac{\lambda_1 - \lambda_2}{\lambda_1}$	(Atik et al., 2021; Hackel et al., 2016; Thomas et al., 2018; Weinmann et al., 2013; West et al., 2004)
	Planarity	$\frac{\lambda_2 - \lambda_3}{\lambda_1}$	(Atik et al., 2021; Hackel et al., 2016; Thomas et al., 2018; Weinmann et al., 2013; West et al., 2004)
	Curvature	$\frac{\lambda_3}{\lambda_1 + \lambda_2 + \lambda_3}$	(Atik et al., 2021; Hackel et al., 2016; Thomas et al., 2018; Weinmann et al., 2013; West et al., 2004)
	Sphericity	$\frac{\lambda_3}{\lambda_1}$	(Atik et al., 2021; Hackel et al., 2016; Thomas et al., 2018; Weinmann et al., 2013; West et al., 2004)
	Verticality	$1 - \lvert \langle [0,0,1] , e_3 \rangle \rvert$	(Hackel et al., 2016)

4.4. Multi-scale approach

An approximation approach was adopted to improve computational efficiency while querying for neighborhood candidates (Hackel et al., 2016). The entire point cloud was iteratively subsampled by dividing it into voxels with a given grid size. Within each voxel, the closest point to the barycenter was preserved, while the rest of the points were discarded. In order to increase the discriminative power of the classifier between objects of different sizes, the geometric features were calculated at multiple scales (Thomas et al., 2018). The different radii for a given scale were derived using the Equation (8).

$$r_{scale} = r_{smallest} * F^s \tag{8}$$

Where r_{scale} is the radius of the current scale, $r_{smallest}$ is the radius of the smallest neighborhood, $s \in \{0, \dots, Total\ number\ of\ scales - 1\}$, and F is the desired growth factor between one scale's radius and the other.

The number of points within the neighborhood, or density, $\rho = \frac{radius}{grid\ size}$, is a crucial metric for balancing between obtaining meaningful descriptions of the structural distribution and computation times. The grid sizes for each scale were calculated with $\frac{r}{\rho}$, where $\rho = 5$ as it showed to result in a good balance between computational performance and discriminative power (Thomas et al., 2018).

Since the buildings of the study area did not possess highly intricate architecture as in the datasets used by other authors (Hackel et al., 2016; Weinmann et al., 2015b), this study used three scales to subsample the point cloud with gradually increasing grid sizes and radii to capture the study area's level of detail (Table 4).

For each scale S_i (where $i = 1, 2, 3$), the respective geometric features were calculated as an array having a length n. Subsequently, the array at each scale was concatenated into one single vector, e.g., Linearity $L = [L_{S_1}, L_{S_2}, L_{S_3}]$ where $L_{S_1} \in [0,1]^{n_1}$, $L_{S_2} \in [0,1]^{n_2}$, $L_{S_3} \in [0,1]^{n_3}$ and $L \in [0,1]^{n_1+n_2+n_3}$.

Similar steps of subsampling, feature calculation, and concatenation were performed for the point cloud for which the machine learning algorithm would be used to predict its classification.

Table 4. Scales at which subsampling and feature calculation were carried out.

Scale	Grid size (m)	Radius of neighborhood (m)
1	0.1	0.5
2	0.2	1.0
3	0.4	2.0

4.5. Classification

Prior to classification, each concatenated feature vector was vertically stacked into one all-inclusive vector v having the appropriate data structure for machine learning. For instance, the concatenated vector Linearity L would form one row and the next row would be Planarity P such that $v = \begin{pmatrix} L \\ P \end{pmatrix}$ where $L = [L_{S_1},\ L_{S_2},\ L_{S_3}]$ and $P = [P_{S_1},\ P_{S_2},\ P_{S_3}]$. This pattern would repeat to encapsulate the whole set of features into v.

In this study, point records with null geometric values were not discarded. However, some feature descriptors were scaled to have a range from 0 to 1 using the min-max scaling Equation (9).

$$x_{normalized} = \frac{x - x_{min}}{x_{max} - x_{min}} \tag{9}$$

Scaling was only applied for the features derived from height values since the eigenvalue-based features and color attributes already ranged from 0 to 1 due to the aforementioned normalization.

4.5.1. Random Forest classifier

The RF ensemble learner was used as the classification model for the study area point cloud. The machine learning classifier was trained with the concatenated feature vector resulting from the reference point cloud and then later the competent RF classifier was used to predict the classification labels for the study area tile. In order to predict the study area tile, the concatenation and stacking methods mentioned in sections 4.4 and 4.5 was applied to the whole tile and the reference point cloud. RF fits the model based on bootstrapping multiple instances of unique decision trees and comes up with decisions according to average aggregations of the tree ensemble, commonly referred to as bagging (Breiman, 2001). Although relative to other classifiers, RF has high training times, it results in high accuracies for classifying 3D point clouds (Atik et al., 2021). Hyper-parameter tuning of the RF classifier's parameters is crucial

to better understanding the data being trained on and having a classifier equipped with good descriptive power. Hyper-parameters, which are user-defined parameters, are data-specific options for balancing between model performance and computation times. Multiple combinations of hyperparameters, such as the number of decision trees, the maximum depth of the tree, the minimum number of samples required at each leaf node, and the minimum number of samples required to split a node, were defined as a grid of hyper-parameters. Using the reference and study area tile, an RF classifier was employed multiple times with several combinations of hyper-parameters. The combinations, or hyperparameter grid, was used to find the optimal values (Table 5).

Table 5. Hyper-parameters used in the grid search for optimal hyper-parameters for the RF classifier.

Number of trees in the forest	Maximum depth of trees	Minimum number of samples to split	Minimum number of samples required at each leaf node
45	10	2	1
50	15	5	2
70	20	10	4

4.5.2. Performance evaluation

In order to assess the performance of the test point cloud prediction, overall accuracy, precision, F1 score, and recall were used. These accuracy metrics rely on the prior splitting of the reference point cloud data into train and test sets. In this case, 80% of the labeled data was entered into the model as training data, while the rest was hidden as test data for accuracy estimation. This was followed by evaluating the predictions with the test sets' labels to measure the proportion of correctly labeled points. Precision and recall per class were calculated with Equations (10) and (11).

$$Precision_{class\ x} = \frac{True\ positives_{class\ x}}{True\ positives_{class\ x} + False\ positives_{class\ x}} \quad (10)$$

$$Recall_{class\ x} = \frac{True\ positives_{class\ x}}{True\ positives_{class\ x} + False\ negatives_{class\ x}} \quad (11)$$

The F1 score is computed as the harmonic average of the precision and recall metrics. The F1 score of each class provides insight into how many times the model predicted a true value and is calculated with the Equation (12).

$$F1\ score_{class\ x} = 2 \times \frac{Precision_{class\ x} \times Recall_{class\ x}}{Precision_{class\ x} + Recall_{class\ x}} \quad (12)$$

Moreover, the RF classifier, grid search, and performance evaluations were used from the extensive and widely used machine-learning Python library Scikit-Learn (Pedregosa et al., 2011).

4.5.3 Criteria

The study area tile was classified multiple times using different RF classifiers to understand the influence of each feature descriptor on the performance of the classification. Each classifier was trained with a limited set of features, i.e., criteria. A criterion could be made up of either just a single feature descriptor (height, color, or geometry), a combination of feature descriptors (e.g., geometric and height features) or the entire feature set. Furthermore, the RF classifier trained with relative height values included the entire feature descriptors. The criteria and their description are outlined in Table 6.

Table 6. Description of the criteria used to limit the feature descriptors and train the RF classifiers.

Criterion	Description
GEO_ONLY	Only geometric features were used
HEI_ONLY	Only height features were used
COL_ONLY	Only color features were used
GEO_HEI	Geometric and height features were used
GEO_COL	Geometric and color features were used
COL_HEI	Color and height features were used
ALL_FEAT	The entire feature set was used with absolute heights
NO_GROUND	The entire feature set was used with relative heights

4.6. Computer resources

The processing of the data was done with the aid of University of Tartu's high performance computing cluster (University of Tartu, 2018). The files were transferred onto the Linux system and the processing was queued and executed using the widely used Simple Linux Utility for

Resource Management (SLURM) workload managing system. The main cluster partition, which possessed 5120 CPU cores and AMD EPYC 7702 processors, was used to run the processing scripts. The criteria were divided into different SLURM jobs, where each job was allocated identical resources, namely, a maximum of 8 days of operation time, 100 GB of CPU core memory with the lack of parallelization since subsampling and feature calculation were dependent tasks.

4.7. Validation of rooftops

Projet Informatique De Cartographie Continue (PICC) is a three-dimensional cartographic dataset collected across the Wallonian landscape. It is managed, validated and kept up-to-date by the geomatics department of *Service Public de Wallonie* (SPW) (PICC, 2024). The dataset is an amalgamation of various geospatial data sources, ranging from data surveyed by the SPW to data from public vendors. A version of PICC is free and open to public use, while the comprehensive version, PICC-vTOPO, is available to partner companies. Both versions are maintained at an accuracy of less than 25-cm. PICC is comprised of topographic, infrastructural, architectural, hydrographic and land use information (Stéphenne et al., 2015).
The PICC dataset that corresponded to the extent of the study area was downloaded and used in this study for validating the result of the classification. Due to misalignment between this study's dataset and PICC resulting from differences in spatial resolution, a one-to-one validation of buildings is not possible. However, this study used a workaround for validating the accuracy of rooftop extraction from the proposed model. The coordinates of the roof points extracted from the multi-scale classification model were evaluated against roof vector information from PICC. A grid of points regularly spaced 20 x 20 meters was generated covering the extent of the study area tile with 676 points (Figure 4). The grid was used to visually register the frequency of true positive and false positive values, i.e., whether the roof points from the classification were aligned with the PICC vector data. Due to the difference in spatial resolution, the roof points located within a tolerance distance of 20 cm from the PICC roof edges were considered as a true positive.

Figure 4. Map of the regularly spaced 20 x 20 m grid of points. The overview zoomed into one of the auditoriums in Croix du Sud shows an exaggerated tolerance distance between the point and PICC roof data.

4.8. Workflow chart

An overview summarizing the previously explained major steps of the multi-scale classification workflow are presented in Figure 5. It includes the key functions, their parameters, the expected input, and output data. The DEM is included in the workflow if the concerned model requires relative height calculation, otherwise a DEM is not needed. Moreover, it shows the validation technique using the grid of points and only the points classified as roof.

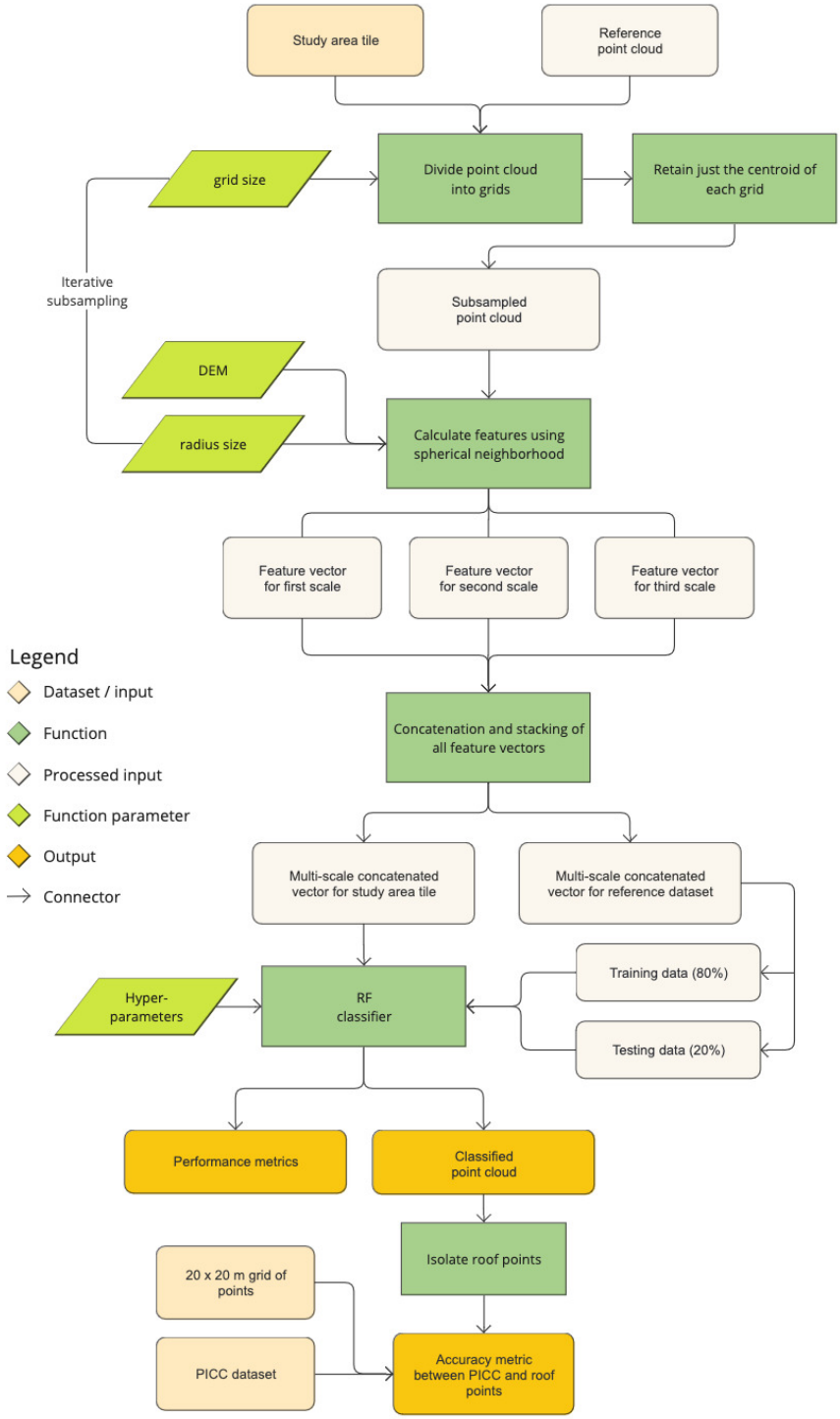

Figure 5. Workflow chart displaying the different inputs, outputs and functions of the multi-scale classification and validation of results. DEM is an optional parameter used for the calculation of relative heights.

Chapter 5. Results

In this chapter, the results of the three major steps of the multi-scale classification are given alongside the validation of the outcome using the PICC dataset. Firstly, an analysis of the subsampling of the point cloud and its influence on point density is presented. Secondly, the distribution of height, color, and geometric feature values plotted according to each classification are displayed. Thirdly, the performance of the classification is presented quantitively and qualitatively. Quantitively, model performance metrics such as overall accuracies, F1 scores and a confusion matrix are presented. Qualitatively, several snippets across the spatial domain of the classified study area are examined to highlight the strengths and weaknesses of the model. Lastly, the classified point cloud is compared with the PICC rooftop dataset for providing a validation of the model's classification of roof points.

5.1. Subsampling of the point cloud

The subsampling of the point cloud was iteratively performed at three progressively increasing grid sizes (0.1, 0.2, and 0.4 meters). The effect of subsampling on a subset at the three scales showed a dramatic decrease in point density (Figure 6). The first scale appeared identical to the initial point cloud, such that the geometric detail of the area is preserved within less than half of the original point density. However, as expected, the sparsity of the points increased as the as the grid size increased and processing time decreased. At the third scale, the subsampling algorithm decreased the point density to less than 5% of its initial density (Figure 6d).

Though structures were simplified into primitive shapes lacking definition, the geometric topography was preserved. For instance, the smaller structures on the rooftops, the detailed markings on the road surfaces, the points representing the window and balcony indentations lost their detailed topographical data and was represented by a smaller collection of sparsely distributed points. Nevertheless, the overall geometry of the ground, facades, rooftops, and the general shape of the vegetation maintained throughout all the scales.

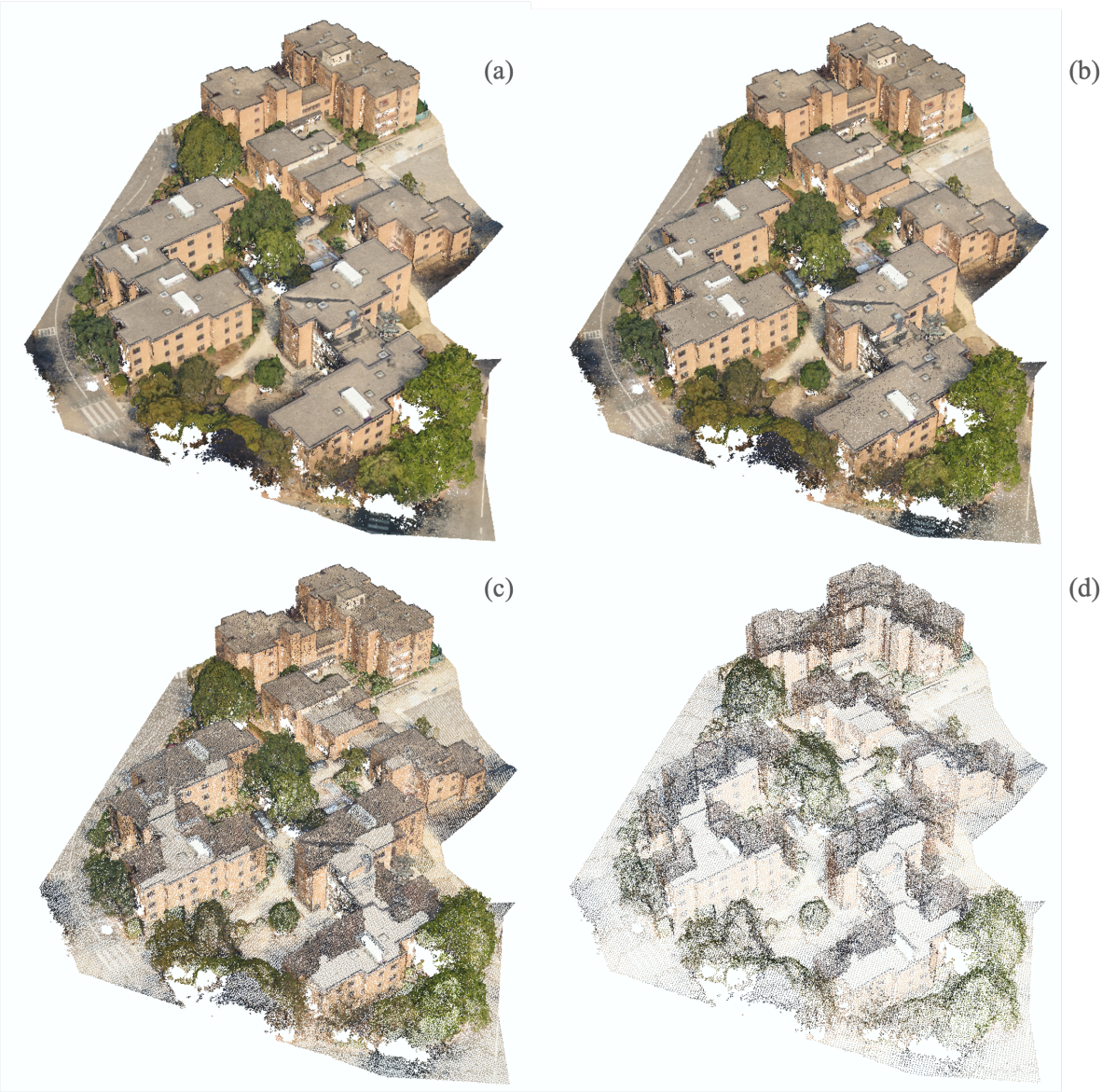

Figure 6. Visual representation of the reduction in point density shown with an exemplary subset of the point cloud (a), subsampled at scale 1 (b; grid size: 0.1m), at scale 2 (c; grid size: 0.2m) and at scale 3 (d; grid size: 0.4m).

After subsampling the reference point cloud and the study area tile, the absolute number of points was decreased by 11,868,133 points and 53,222,549 points respectively. Alternatively stated, the number of points in both the reference point cloud and the study area tile was reduced by ca. 40%. The subsampling of the finest scale took 9.5 minutes to reduce the point density of the entire study area, while both the intermediate and coarsest scale subsampled the point cloud in 4 minutes and 2 minutes, respectively. Figure 7 illustrates this reduction and further shows that the finest scale, allocated the larger portion of the subsampling, while in both the reference and classified point clouds, the subsampling at the coarsest scale possessed a fraction of the initial point count, specifically, they accounted for less than 3% of the total number.

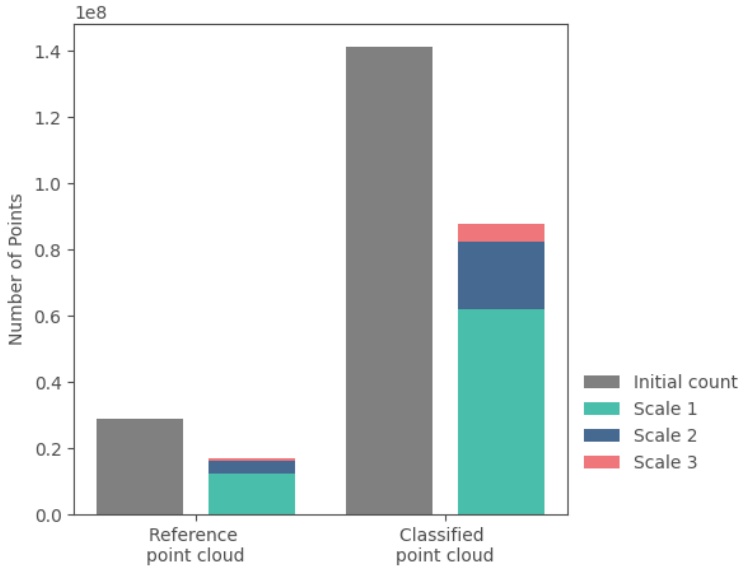

Figure 7. Graph showing the reduction in the number of points after subsampling using the voxel-grid method.

Expectedly, the density of points also decreased at every subsampling iteration (Figure 8), where the classified point cloud had initially a point density of ca. 548 points/m^2 and the training point cloud had ca. 315 points/m^2. At each subsampling scale, the point density of the classified point cloud was slightly higher than that of the reference point cloud. Within the last scale, both point clouds shared the least difference between point densities, having a point density of 11 points/m^2 for the training cloud, while the classified point cloud had a point density of 21 points/m^2.

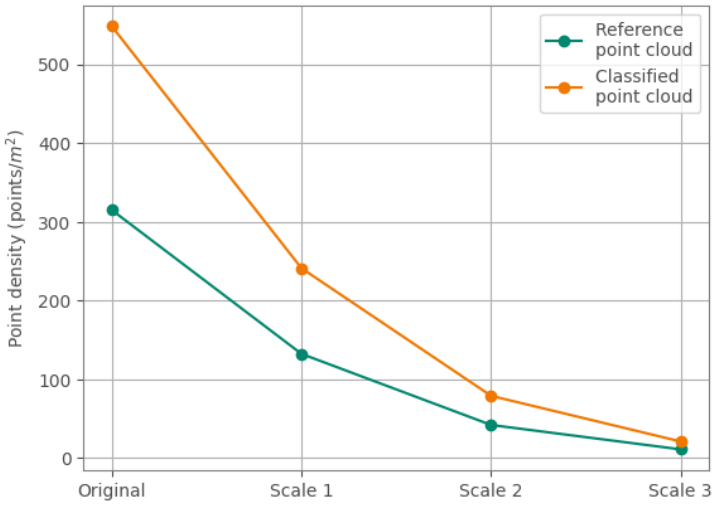

Figure 8. The original point densities and the densities at each subsampling scale for the reference point cloud (green) and the classified point cloud (orange).

5.2. Topography of classified point cloud

The absolute height values, which represents each points' altitude from mean sea level, ranged between 125.4 meters to 189.3 meters. The majority of the values ranged between 141 meters and 149 meters. The lowest elevation values were found on the northwest. An increasing height gradient could be observed running diagonally towards the southeast. Trees seemed to be the highest structures with points ranging between of 140 and 178 meters. Besides ground points, the structures with the lowest elevations were vehicles and short vegetation (such as landscaping bushes and shrubs) (Figure 9). Though trees possessed the top range of height values, the structure with the highest altitude (189.3 meters) was a slender antenna situated on one of the rooftops in the eastern end of the study area tile.

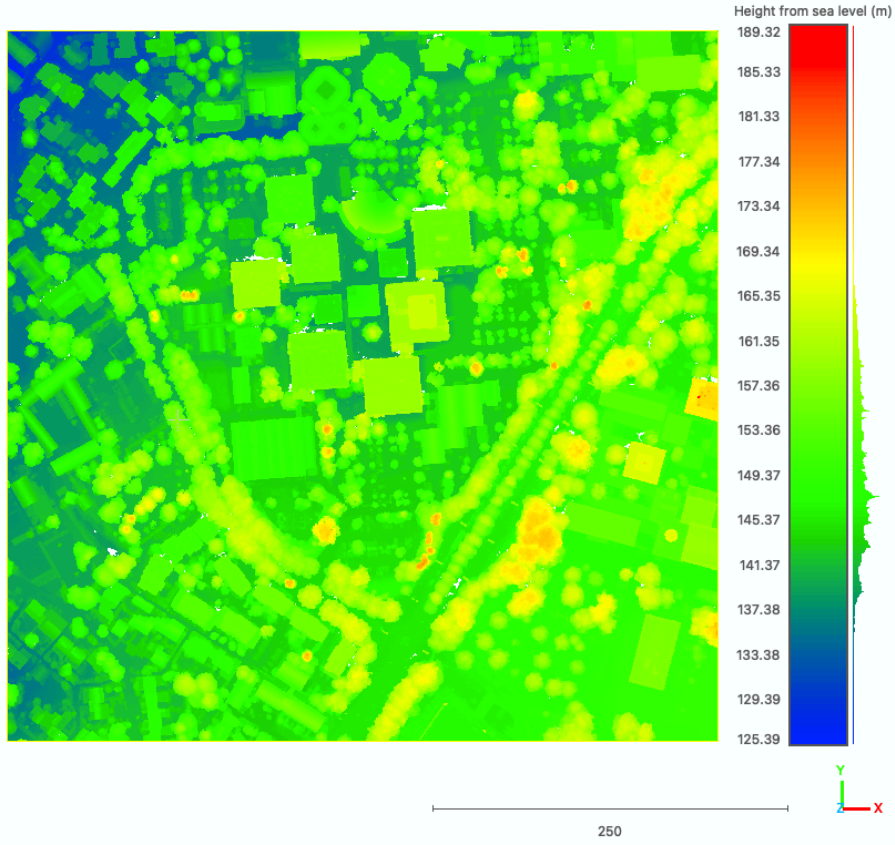

Figure 9. Elevation map of the classified point cloud, where the absolute heights are presented in meters.

5.3. Density distribution

Using three spherical neighborhoods (0.5, 1 and 2 meters), descriptive features were calculated for each point. In addition, results of the classification provided with each point a semantic label (ground, vegetation, roof, facade, or vehicle). Consequently, the density distribution of the points according to the different features could be reviewed in detail per classification.

5.3.1. Height features

The height values computed for each neighborhood are normalized values ranging from 0 to 1 using the min-max scaling formula.

Figure 10 displays the distribution of each points' average height of the neighborhood (labelled as height mean), the difference between each point and the lowest point in its neighborhood (height below) and the difference between the highest point in the neighborhood and each point (height above).

The height below and height above attributes shared a similar distribution, such that two peaks in the density was observed, where the peak of the lower values were attributed to ground and roof points and the peak of the higher values were attributed to facade and medium vegetation. However, the average height values showed a more sporadic distribution with density values creating multiple peaks and valleys. Nevertheless, a clearer distinction is observed between the average height values of the ground points, facade, and vegetation points. This distinction is displayed in the form of a shift between the distribution density of the classes, showing that the higher values are unique to the medium and high vegetation points, while the lowest values were unique to ground points. The highest roof points' density was mainly found in the mid-range between 0.2 and 0.6, overlapping with vegetation and facade points.

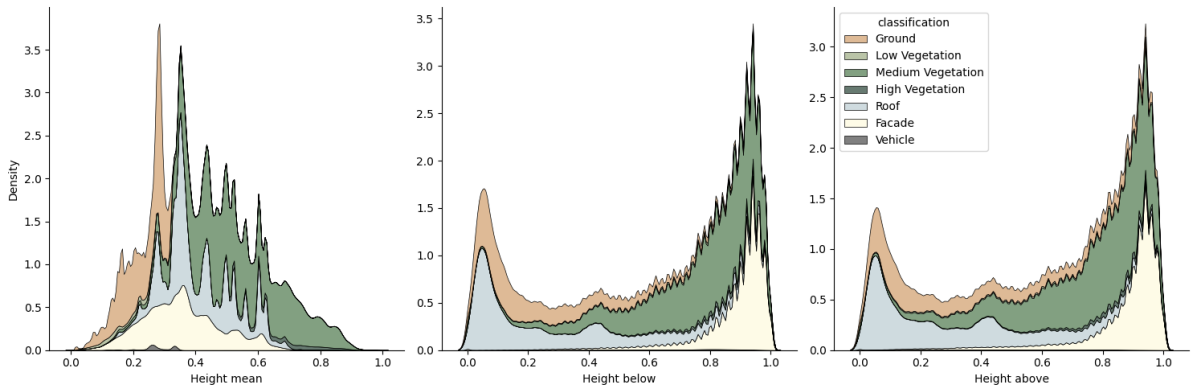

Figure 10. Density distribution of the normalized height attribute at each point's neighborhood. Namely, average height (left), height below (middle), and height above (right).

In contrast, the average relative height of each point extracted from the difference between the ground elevation and the points' elevation display a distribution that is different from the average absolute height values (Figure 11). Prior to normalization, the relative heights ranged from ca. -7 meters to approximately 43 meters (Figure A1). There exists less fluctuations in the density and a slight shift from low height values to higher heights, where facades and roofs had the highest density of low height values and low and high vegetation had a higher density at the

higher values. The distribution density of facades peaked at a height value of 0.15 and had a smooth decrease as average height values increased. Medium vegetation had also a peak in distribution density at the lower height levels and existed throughout the distribution curve in lower densities. It is noteworthy that the density of high vegetation became the predominant vegetation class when elevation was converted to relative heights.

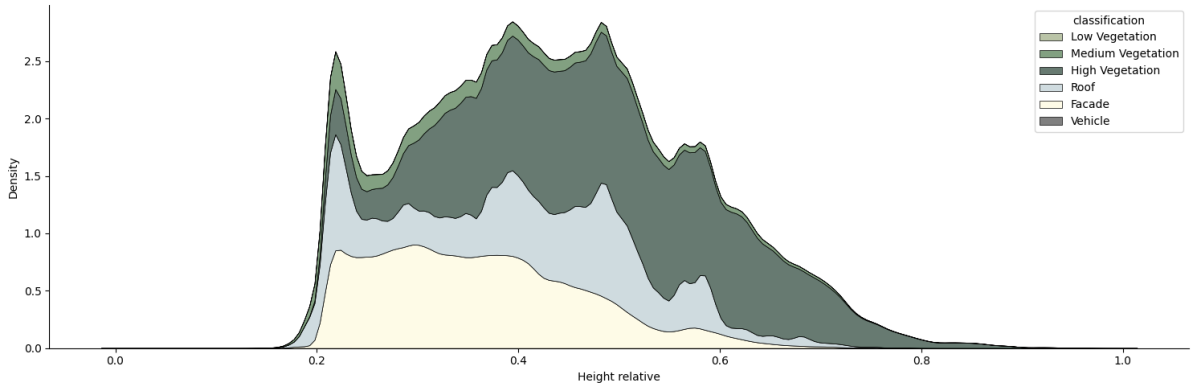

Figure 11. Density distribution of each point's normalized relative height value calculated using a reconstructed DEM of the study area tile.

5.3.2. Color Features

The reflectance information of the dataset, which was initially expressed in the red, green, blue (RGB) spectrum, contained a similar distribution across the different classification labels (Figure 12). Most notably, facades, vegetation and ground labels possessed a similar distribution, where the density reaches a rapid peak at the lower values (ca. 0.15) then gradually decreased to a null density at the higher color values. Ground points maintained the highest distribution density across the color space while vehicles and facades remained to have the lowest densities. The density of rooftop values displayed a similar pattern across the spectrum, where its values were predominant in the mid-ranges. However, only within the green spectrum, roof points displayed two peaks at 0.2 and 0.4 followed by a gradual descent mirroring the rest of the distribution. Within the blue spectrum, the distribution pattern remained the same, while a minor secondary peak occurred at ca. 0.5 with ground, medium vegetation, and roof labels.

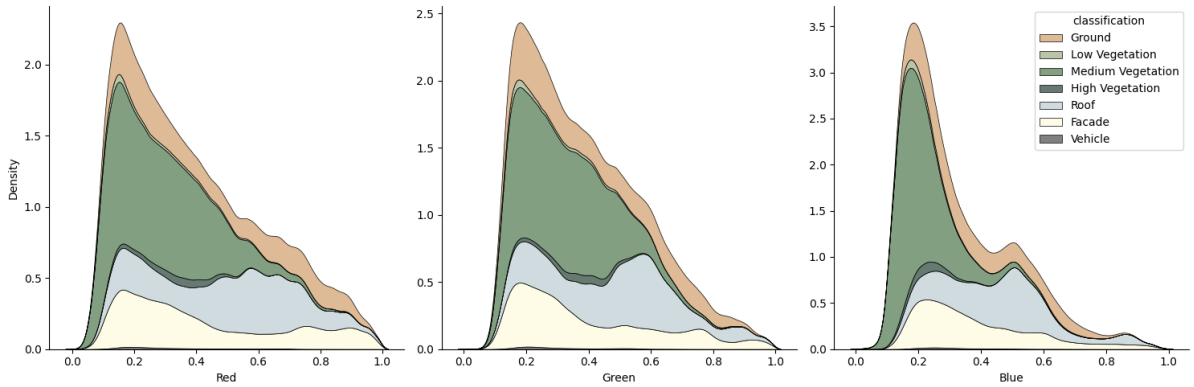

Figure 12. Density distribution of the R (left), G (middle), B (right) color values according to the classification.

When the reflective values were converted to the hue, saturation and value, each domain contained a vastly different distribution in comparison to the RGB space. Regarding hue values, three separate peaks in density of distribution was observed. The first peak, which pertained to the highest density, occurred at hue value of around 0.1 and was attributed to points classified as roof, facade, medium vegetation, and ground. They displayed a secondary minor peak at around approximately 0.6, where the density was half of the primary peak. Another peak was seemingly unique to medium vegetation occurred at ca. 0.25 (Figure 13; left).

The saturation distribution reached its highest density rapidly and simultaneously for all classification labels at very low values of saturation. Followed by a gradual decrease to null density. In contrast however, the descent was not simultaneous between the labels. The density of roofs and facades decreased first, followed by a rapid decrease in ground points' density. Finally, the distribution of medium vegetation was separated from the rest with an isolated decline (Figure 13; middle).

The distribution of value density, while similar to that of the saturation density, contained a notable difference in patterns for roofs, facades, and low vegetation labels. They increased rapidly as with the other labels, but a plateau was reached at around 0.5 where they kept their density fairly constant, before rejoining the similar pattern of a descent to null at the higher values (Figure 13; right).

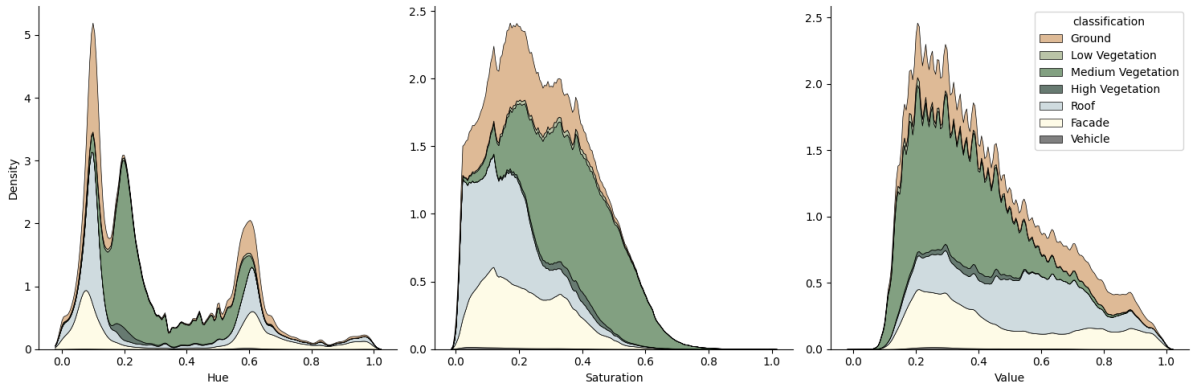

Figure 13. Density distribution of the H (left), S (middle), V (right) color values according to the classification.

5.3.3. Geometric features

The density of geometric features pertained mainly to points classified as ground, medium vegetation, roof, and facade, while points classified as vehicle and low vegetation did not possess a notable density. Moreover, ground points and medium vegetation points shared the larger portions in density as opposed to roof and facades. All the calculated geometric features had at least one peak in density and most geometric features tended to have the same pattern of rise and descent per classification.

Ground and roof points reached a maximum density of ca. 4.5 and ca. 3.5 respectively in the low ranges of the omnivariance distribution. Then ground classification decreased rapidly to join the gentle ascent with medium vegetation to reach a secondary maximum, while roof points decrease to join facade labels to plateau across the intermediary omnivariance values. After an omnivariance value of 0.32, all labels reach a null density (Figure 14a).

Eigenentropy's distribution maintained a null density until a value of 0.6 for all classes, after which facade, roof and ground labels increased at a rapid rate to maximum density of approximately 14, followed by a sharp decrease with a similar rate to a density of 2.5, where they joined medium vegetation points and plateaued throughout the higher eigenentropy values (Figure 14b).

The distribution of anisotropy was mainly contained to the higher anisotropic values. Medium vegetation and ground labels showed a slow and progressively increasing density prior to a sharp rise to reach their peak. Roofs and facades had a similar slow ascent, but to a lesser extent, and combined with the rest of the labels to reach their maximum density at the higher values (Figure 14c).

The density values of linearity displayed a positive skew, where the density increased with a rapid rate at first reaching a maximum at a linearity value of 0.1. Then the density decreased to null at a linearity value of ca. 0.8 (Figure 14d).

The density of planarity values displayed a distribution that was the mirrored opposite of the distribution of linearity. The values of the density of planarity were skewed negatively, i.e., the highest density was found to be attributed with higher planarity values (Figure 14e).

Curvature values reached a peak density almost immediately. It was centered around 0 with a sharp decline back to lower densities. Followed by a steady decrease along the mid-ranges of curvature values. Medium vegetation labels predominated the mid-ranges, after around 0.25 all labels reached null density, making curvature and omnivariance the only distribution ranges to end before the maximum normalized range of 1 (Figure 14f).

Sphericity had a similar pattern to curvature and an opposite distribution to anisotropy. A sharp rise occurred immediately making its peak centered around 0, then a similarly sharp decrease caused the density of most labels to reach a null at 0.2, except for medium vegetation which reached its null at 0.4 (Figure 14g).

The verticality distribution showed that, similar to curvature and sphericity, it had a peak in distribution centered around 0, however the peak pertained to only roof and ground points. Medium vegetation points were predominant across the mid-range values of verticality, albeit at a lower density. At the highest verticality values, a smaller but noticeable peak in density was observed, being unique to medium vegetation in combination with facade points (Figure 14h).

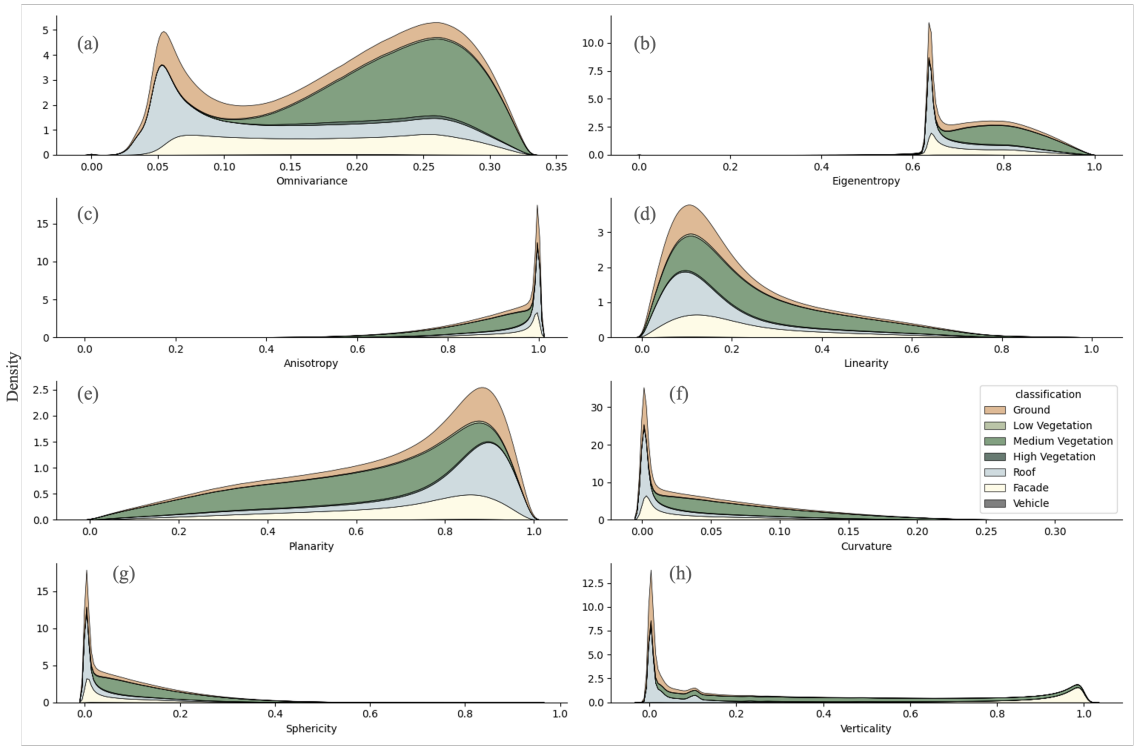

Figure 14. Density distribution of geometric features extracted from the classified point cloud.

5.3.4. Feature calculation time

The time taken for calculation of each feature showed that height and color features had similar timings, while geometric features took more than double the time to process for each point (Table 7; see section 4.6 for computer specifications). It is noteworthy that, the difference between relative and absolute height calculation times for iterated point itself is null, however calculating the relative height for all points in each neighborhood took more than 6828.26 minutes, or 4.7 days (Table A1). Expectedly, as the radius of the querying sphere grew, the time it took to process each feature decreased considerably since less iterations were required to cover the study area. The first and smallest radius taking 81 minutes having as high as 46.86 minutes for geometric features and as low as 16.22 minutes for color features, whereas the third and largest radius taking less than 10 minutes. Hence this part of the workflow alone took in total 118 minutes to run.

Table 7. Time (in minutes) taken for the calculation of geometric, height and color features for the study area tile at each scale, where the spheres' radii were 0.5, 1 and 2 meters.

Feature	Scale 1	Scale 2	Scale 3	Total time (min)
Geometric	46.86	16.61	4.70	68.17
Height	18.13	6.49	1.86	26.47
Color	16.22	6.11	1.75	24.08
Total time (min)	81.20	29.20	8.31	118.72

5.4. Performance metrics

The results of the multi-scale point cloud classification model are presented for each criterion mentioned in section 4.5.3. The analysis of the performance is specific to the study area and its innate geometric and physical attributes. The testing points consisted of 20% of the reference dataset, which were hidden from the classifier during the training process, were used to yield accuracy measures for the model limited by each criterion.

5.4.1. Hyper-parameter tuning

A grid search was used to exhaustively search for the most optimal values for the hyper-parameters using the reference point cloud and the study area tile. The grid search resulted in the following optimal values for the model: 100 trees in the forest, no maximum depth, 1 minimum number of samples, and 2 minimum number of samples for a split. The aforementioned hyper-parameter values resulted in a 95% overall accuracy, consequently ranking the highest among other different combinations of values. However, the number of

trees in the forest was reduced to 50 trees as a tradeoff between training accuracy and training time.

5.4.2. Accuracy of model

The overall accuracy of the model returns an overview of the ratio of predicted to actual classes within the reference point cloud. In general, semantic classification based on solely a single feature resulted in lower accuracies for predicting unseen data, while the combination of multiple feature descriptors resulted in accuracies of 0.86 and above (Figure 15).

The criterion with the lowest accuracy was the classifier trained only using geometric features (GEO_ONLY), returning an accuracy of 0.59, while the classifier trained with all features and without ground points resulted in the highest accuracy of 0.95 (NO_GROUND). Models trained on either height or color criteria surpassed the predictive accuracy of GEO_ONLY, where the latter criterion performing slightly better (0.73). In contrast, the ALL_FEAT criterion, which was trained on using all three feature sets, including ground points, resulted in an overall accuracy of 0.94. Interestingly, the classifier trained on color and height features (COL_HEI) produced a similar accuracy of 0.93 outperforming GEO_COL criterion, which was the model trained using geometric features combined with color features (0.86) and the model trained using geometric and height features (GEO_HEI) (0.79).

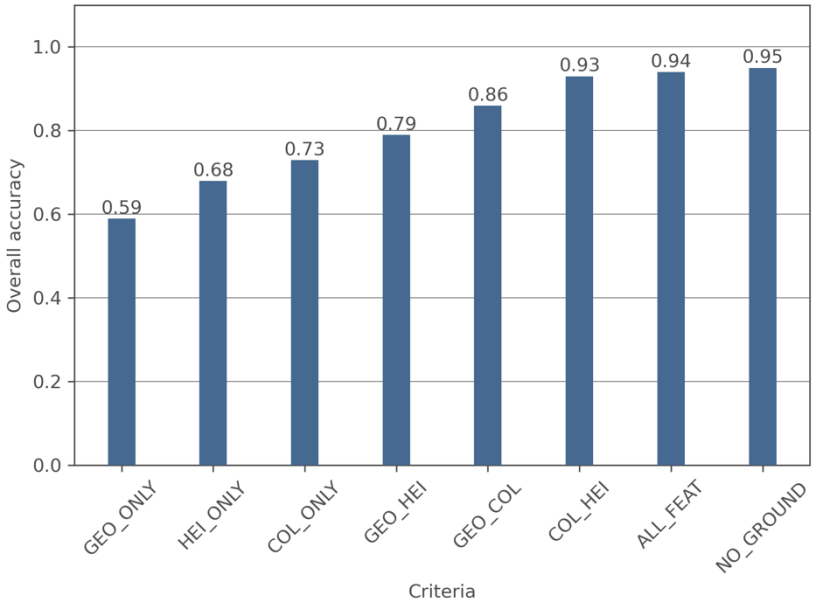

Figure 15. The overall classification accuracy for each criterion, i.e., for each combination of feature descriptors.

5.4.5. Confusion matrix

The utilized RF model is a supervised model with portion of the reference point cloud used for evaluation of the model's performance. Therefore, a multi-class confusion matrix was used to display the label-wise distribution of the model's predictive performance in contrast to the actual training points within the reference point cloud.

While ALL_FEAT and NO_GROUND returned similar confusion matrices, Table 8 shows only the tabulated percentage of points correctly classified by the model with the ALL_FEAT criterion to evaluate the performance of classification using absolute height values combined with color and geometric features (Refer to Table A2 for absolute values). The overall accuracy for this criterion was 94%, hence the largest share of test points was classified correctly for all labels. Generally, ground, medium vegetation, roof and facade structures were well described by the features used for classification as more than 90% of their points were properly classified. High vegetation label was seen to experience the highest degree of confusion with medium vegetation, where almost half of the test points (51.12%) were misclassified as medium vegetation. However, high vegetation shared indiscernible misclassifications with other classes. Vehicles were conflated with almost all other labels except for high vegetation. A portion of vehicle test points (ca. 10%) were especially misclassified as ground due to both labels possessing similar elevations. Furthermore, the planar distribution of vehicles' sides and roofs were expectedly confused with facades and rooftops due to their similar geometric properties. Building features (roof and facade labels) shared some confusion between each other where 3% of facade points were misclassified as roof and almost 2% of roof points were misclassified as building facade. Moreover, ground points shared a noticeable confusion with all classes except high vegetation.

Table 8. Confusion matrix (in percentage) for all features (ALL_FEAT criterion) that includes the predicted classes by the classifier as columns compared against the row-wise actual classes from the reference point cloud. The values have been normalized by dividing each value by the row's total.

		Predicted class						
		Ground	Low Vegetation	Medium Vegetation	High Vegetation	Roof	Facade	Vehicle
Actual class	Ground	96.56	0.94	0.92	0	0.42	1.06	0.10
	Low Vegetation	8.11	72.74	16.39	0	0.30	2.39	0.07
	Medium Vegetation	1.31	0.59	97.16	0.11	0.15	0.68	0.01
	High Vegetation	0.08	0.02	51.12	48.54	0.05	0.11	0.08
	Roof	2.70	0.22	0.46	0	93.51	3.04	0.07
	Facade	0.85	0.41	0.92	0	1.90	95.90	0.03
	Vehicle	10.75	1.74	2.74	0	3.43	6.15	75.18

5.4.3. Precision and Recall

In this case, the classes were unbalanced, therefore, precision and recall provided a detailed analysis for each class. Mean class precision was 93.6%, while mean class recall reached 82.8%. Precision values by class from the ALL_FEAT criterion showed that all but one class had a precision of larger than 90%. In contrast, recall values ranged from 47% to 97% (Table 9). Roof classes had the highest precision value (96.7%), while medium vegetation recorded the highest recall of 97.25%. Most notably, although high vegetation class recorded a high precision value of 94.95%, it had the lowest recall value registering at 47.46%.

Table 9. Precision and recall measurements (in percentage) derived from ALL_FEAT criterion's confusion matrix.

Class	Precision (%)	Recall (%)
Ground	92.97	96.65
Low Vegetation	88.89	72.83
Medium Vegetation	93.80	97.25
High Vegetation	94.95	47.46
Roof	96.70	93.81
Facade	94.34	95.89
Vehicle	93.54	75.71
Mean	9359.86%	8280.00%

5.4.4. F1 scores

The F1 score also provided a deeper insight into the performance of each criterion by combining precision and recall metrics. It gave a score to each label based on the model's discriminating capability (Figure 16; the tabulated F1 scores are presented in Table A3). Generally, high vegetation and vehicle classes scored the least F1 scores at each criterion, while medium vegetation, ground, roof, and facade classification ranked at being the better structures to be discerned by each criterion. Expectedly, the more feature descriptors the model was trained on, the better the F1 scores. Interestingly, while geometric features performed the worst out of all the criteria, their combination with either color or height features considerably improved the model's discriminative power especially with facade and roof points.

When the model was trained on a sole set of features, facades and medium vegetation points were able to be distinguished well with the GEO_ONLY model (RF classifier trained solely with geometric features). However, vehicle, high and low vegetation labels suffered the worst out of all the criteria registering scores as low as 0.07 for low vegetation and 0.01 for vehicles. Particularly, medium vegetation did not follow this pattern and registered a score of 0.66 comparable to that of the HEI_ONLY criterion (RF classifier trained solely with height features). The criterion HEI_ONLY was notably better at performance when compared to GEO_ONLY, where more than four labels scored more than 0.6. Ground points scored 0.8, a score not reached by any label with the GEO_ONLY criterion. In contrast, the model trained on just color features, exhibited a very high F1 score for medium vegetation (0.87). While facades reached a 0.73 score with COL_ONLY (RF trained with only color features) similar to GEO_ONLY (0.7), roofs were best distinguished with the HEI_ONLY criterion when the model was trained on just one set of features.

Except for when all features were combined to train the classifier, ground and roof labels scored highest when the RF classifier was trained solely with geometric and height features (GEO_HEI). When color and geometric features were combined (GEO_COL), the score of facade points improved greatly reaching a score of 0.92. Vehicles had also scored 0.49, an increase over all the sole criteria and over the COL_HEI criteria (RF trained with both color and height features). On the other hand, the combination of color and height features did not contribute to an improvement of roof and facade scores, having a score identical to that of COL_ONLY criterion, 0.72 and 0.73 respectively.

The model trained with all features (ALL_FEAT), including ground points, scored higher than 0.8 on almost all labels except for high vegetation which resulted in a score of 0.63, yet this score is among the highest only outperformed by NO_GROUND criterion (RF trained with all features excluding ground points). Ground, medium vegetation, roof and facade labels scored an identical score of 0.95 with the ALL_FEAT criterion, slightly lower than that of NO_GROUND scores. Although marginally performing better than ALL_FEAT criterion, the NO_GROUND criterion was able to output unequivocally the best scores for each classification label. Medium vegetation, facade and roof points received an almost perfect F1 score (0.96), yet high vegetation recorded an F1 score of 0.63.

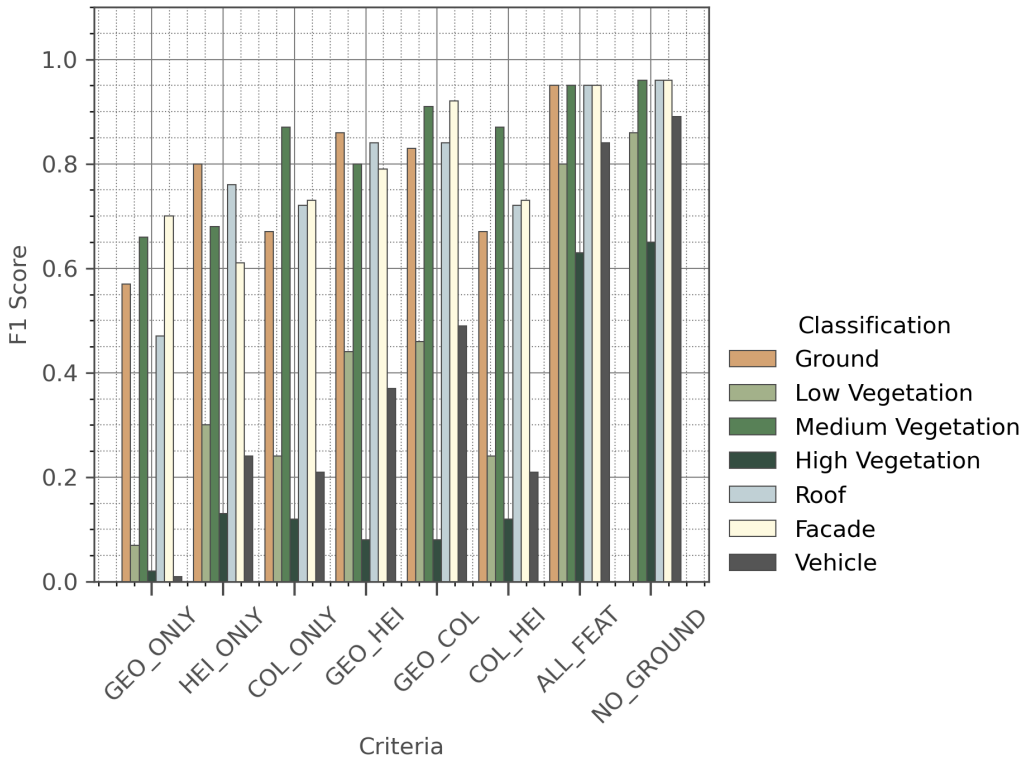

Figure 16. F1 scores of each classification per criterion.

5.5. Classified results of the study area tile

According to the classifier, over a quarter of the points in the classified point cloud represented ground points, while almost half of the points were a type of vegetation. Whereas facade and roof points each made up ca. 13% of the points with the ALL_FEAT criterion. Expectedly, vehicles and low vegetation shared a very minor portion (Figure 17; left). On the other hand, when the ground points were removed, the NO_GROUND criterion showed that more than 60% of the area was vegetated, with 18% of the points representing facade and approximately 21% was allocated for points classified as roof (Figure 17; right).

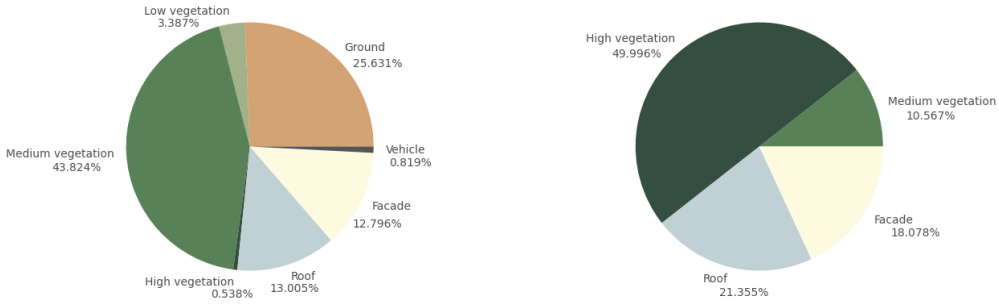

Figure 17. Proportion of classified labels from ALL_FEAT (left) and from NO_GROUND (right).

Aside from the roof points, which were validated with the PICC dataset, a qualitative examination along the classified point cloud tile was done to provide a validation of the model's performance using visual interpretation of whether the model predicted correctly or not. Only the best performing models were considered for this analysis, namely the model trained with all the features (ALL_FEAT) and the model trained with relative heights (NO_GROUND).

5.5.1. ALL_FEAT criterion (with ground points)

Overall, the model was capable of pinpointing most buildings' facades and rooftops alongside vegetation and vehicles. However, some misidentifications occurred within actual ground points and roof tops mainly. Mostly roads and parking lots were misclassified as rooftops, while one building had its unconventionally shaped roof classified as vehicle points (Figure 18).

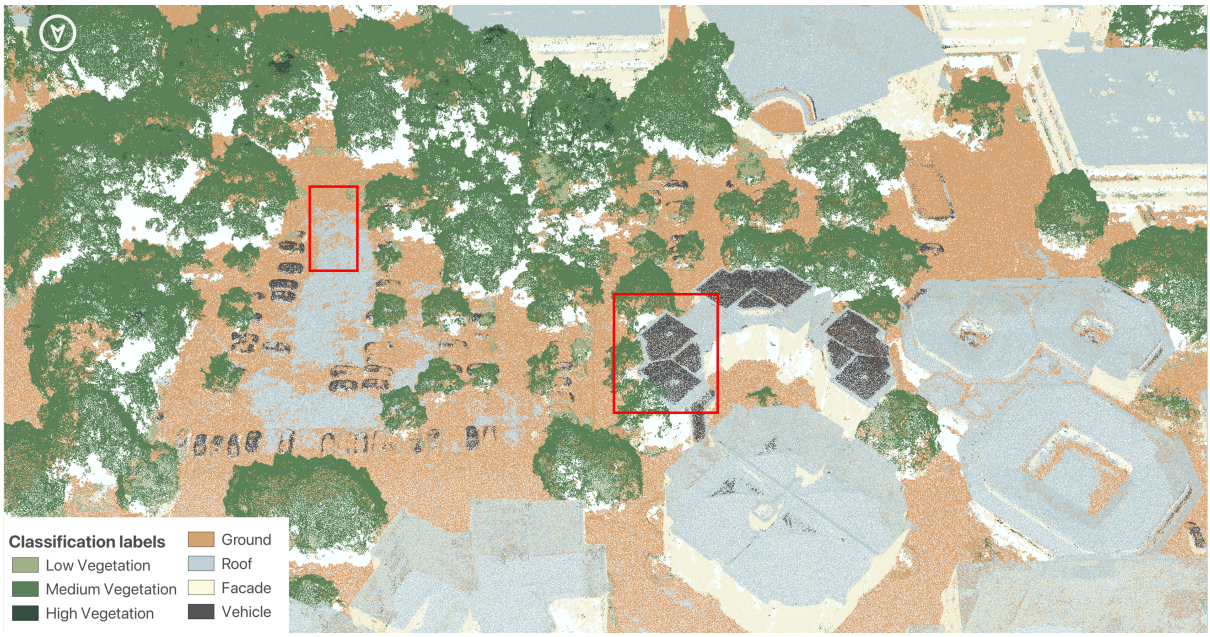

Figure 18. ALL_FEAT classified point cloud perspective showing ground and car inconsistencies (marked in red).

Most frequently, roofs were misidentified as ground points. For instance, in the northwestern part of the study area, many of the rooftops, either entirely or partly, had their roofs infested with ground points (Figure 19).

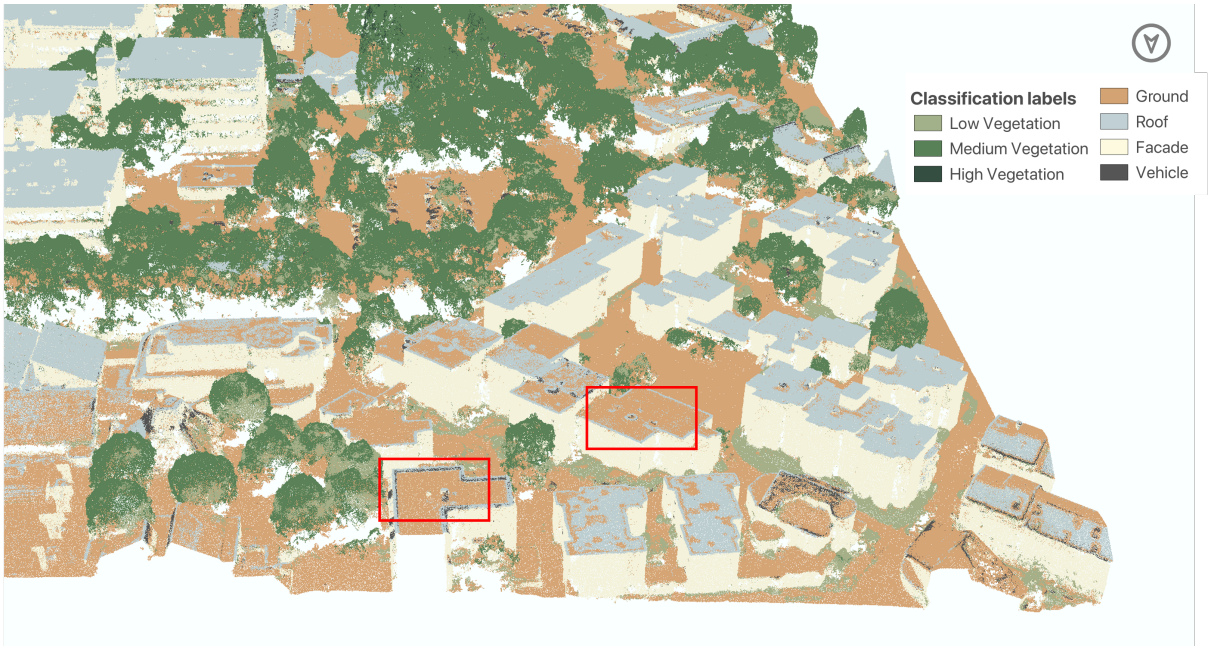

Figure 19. ALL_FEAT classified point cloud showing roof and ground inconsistencies (marked in red).

While vegetation had few and unobservable confusion with built structures, the transition between low to high vegetation was not consistent throughout the study area, with some trees

having their tips allocated for high vegetation despite others of the same height remaining within the medium vegetation class (Figure 20).

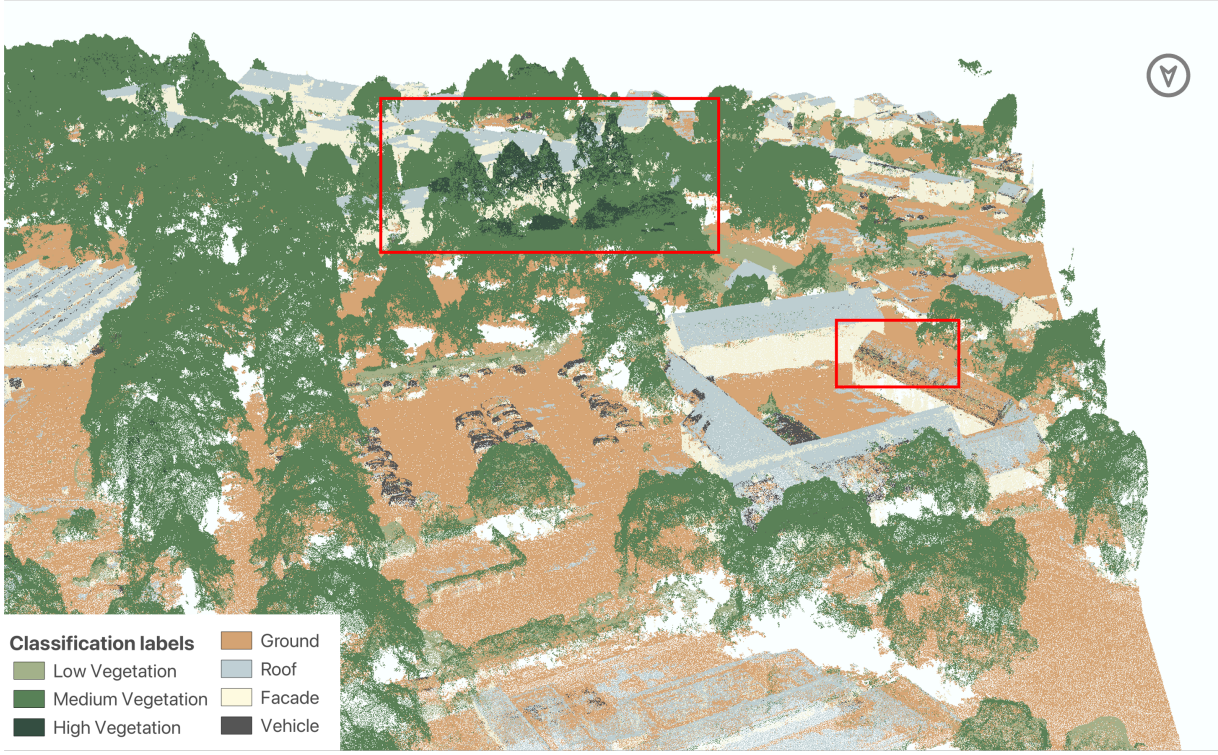

Figure 20. ALL_FEAT classification displaying inaccuracies with roof and vegetation (marked in red).

5.5.2. NO_GROUND criterion (without ground points)

The extraction of roofs with the NO_GROUND criterion was expectedly capable of classifying roof points more accurately as opposed to the ALL_FEAT criterion due to the lack of ground point confusion. However low height points were misclassified as roofs (Figure 21). Nonetheless, it is observable that the performance of NO_GROUND surpassed that of ALL_FEAT since the buildings of the northwestern area with lower elevations, were classified into roofs and facades more distinctly.

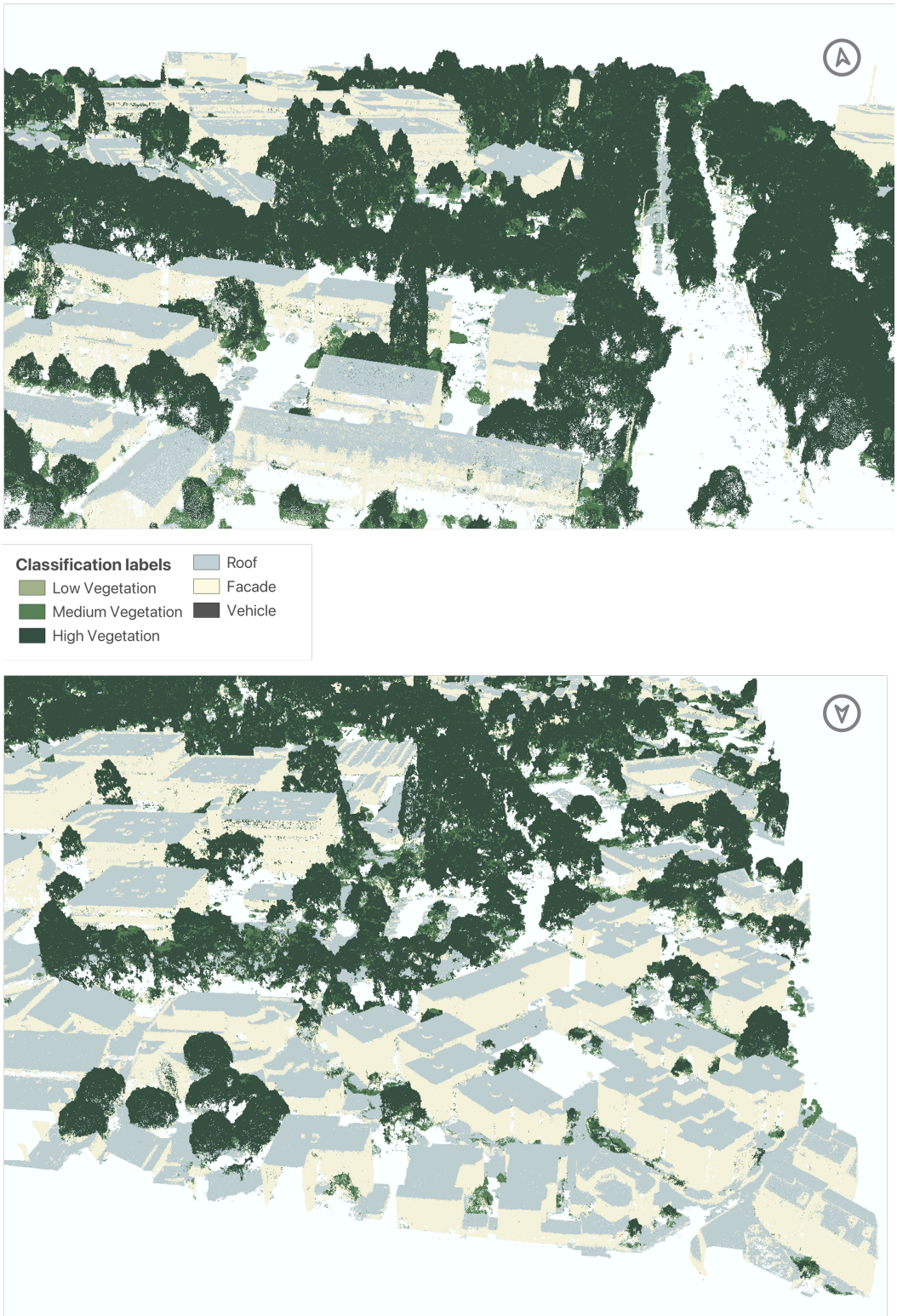

Figure 21. NO_GROUND point cloud perspectives showing the enhanced roof and facade classifications.

However, upon further inspection, vehicles almost ceased to be discerned since they were classified as facades, when the points were organized vertically and roof when the points were configures on a horizontal plane. Moreover, a higher degree of confusion was observed between the vegetation classes, since almost all vegetation was classified as high vegetation.

Nevertheless, beyond the confusion within the classes dedicated to vegetation, the study area's greenery was adequately represented with the NO_GROUND criterion as well since little-to-no confusion was observed with the rest of the labels. Infrequently, tilted roofs were imperfectly classified as facades when the plane lied more vertical than horizontal (Figure 22).

Figure 22. NO_GROUND classification showing vegetation and vehicle inconsistencies (marked in red).

5.5.3. Training and predicting time

The processing time took to train each RF model with different criteria and the time took to predict the classification of the points from the study area are presented in Table 10. Training the model on average took more time than predicting the points since the average training time was approximately 74 minutes, while the average predicting time was around 12 minutes. The fastest criterion to be trained was HEI_ONLY, whereas the criterion which took the least time to predict the study area tile was ALL_FEAT. However, ALL_FEAT was one of the top slowest criteria to train the classifier.

Table 10. Time (in minutes) took to train the RF classifier and predict the study area tile.

Criteria	Training time (min)	Predicting time (min)	Total time (min)
GEO_ONLY	89.48	21.89	111.37
HEI_ONLY	31.88	11.03	42.90
COL_ONLY	39.73	19.31	59.04
GEO_HEI	112.48	11.40	123.88
GEO_COL	80.51	10.77	91.27
COL_HEI	47.39	7.64	55.03
ALL_FEAT	96.14	6.77	102.91
NO_GROUND	97.13	12.06	109.20

5.6. Validation of roof points

The consistency of the roof points with the PICC dataset was compared between the points which were classified as roof with the NO_GROUND criterion to avoid the misclassification taking place between ground and roof. Following a visual analysis, the threshold suitable for representing the misclassified roof points was deemed to be 0.17 (i.e., 1.35 meters). The density of the roof's height points relative to the ground showed that the threshold removed the highest peak of the distribution keeping only 75% of the data (Figure 23).

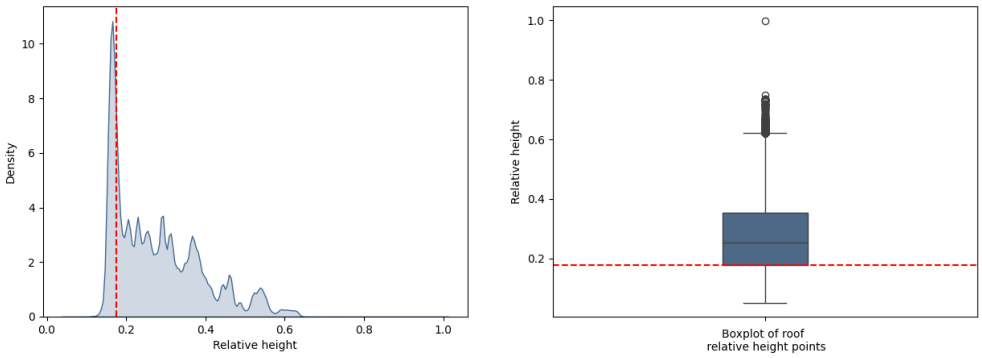

Figure 23. Density distribution of the normalized relative heights for points classified as roof (left) and their boxplot representation (right). The dashed red line represents the cut off value where the threshold was applied for post-processing.

The post-processing procedure of applying a threshold to cut off the misclassified roof points by removing the lower relative heights between 0 and 0.17 increased the overall accuracy from the validation grid from 74% to 91% after post-processing. Based on visual analysis, the approximately 11,000,000 discarded points consisted mainly of vehicle roofs, points representing road or ground, which were undetected by CSF during ground removal (Figure 24a). Moreover, remnants of low height vegetation and other misclassified points were also

removed by the threshold. However, the threshold did not completely remove non roof points since some remnants of higher height vegetation and some ambiguous class points remained even after the threshold due to their height leaking through the cut-off limit (Figure 24b).

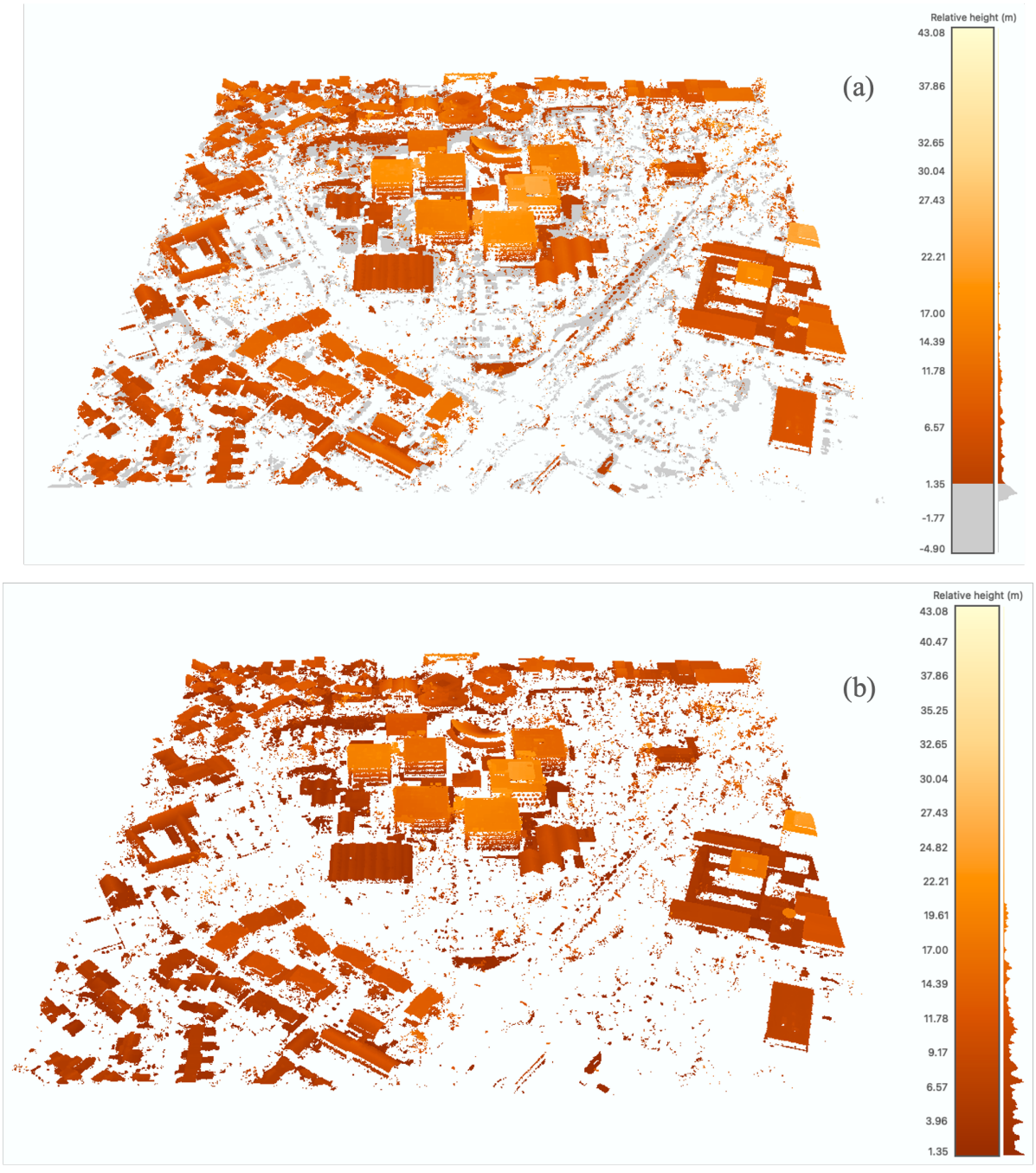

Figure 24. Classified roof points before (a) and after (b) removal of points below the threshold value (grey points).

Chapter 6. Discussion

This chapter provides a synthesis of the key results and an in-depth interpretation of the significance of the results. Furthermore, the limitations of this study and key recommendations for future research avenues are presented. The purpose of this research was to gain an understanding of which features influence the classification of buildings in an urban setting using a supervised classification technique.

The use of multi-scale classification of a point cloud included several intermediary steps for extracting points that which represent buildings' rooftops and facades. Aside from the meticulous task of manually classifying representative subsets from the dataset, computationally intensive steps such as subsampling, point-wise iteration for feature calculation, and prediction using machine learning algorithms are complicated yet effective steps for extracting semantic meaning from point clouds. The simplification of the point cloud showed to reduce computation intensity, while limiting loss of detail. While geometric features alone proved to be inadequate at semantic classification, their combination with color and height features ultimately became the most efficient method for building information extraction in an urban city as Louvain-la-Neuve. If the study area possessed buildings with similar sizes and reflectance values, most geometric features could be skipped altogether as a tradeoff for computation efficiency. Nevertheless, relative height calculation coupled with geometric features, namely verticality information, extracted the most meaningful information when building information is considered the scope to the study. Finally, the photogrammetric point cloud data used showed to have great capacity for vegetation extraction

6.1. Subsampling

By requiring neighborhood features, each point needed to be iterated over to retrieve its neighborhood. Hence, the processing efforts linearly increased as the point count increased (Hackel et al., 2016). As grid size of the voxel grid algorithm determined the resolution of the subsampled point cloud, the sizes chosen within this study showed two key benefits. Firstly, subsampling is excellent at preserving the overall shape of the structures, while simultaneously reducing the number of the points to improve computational efficiency (Figure 6). Secondly, subsampling did not add a superfluous amount of computation times to the workflow. Therefore, it is evident that simplification of a point cloud is one of the most important steps for neighborhood querying since the shapes of structures such as buildings and vegetation are preserved while reducing point count. Even with the coarsest voxel grid size of this study (0.4

m), the structural definition of the classes was maintained and was enough for the classifier to discriminate between the structures. This is mainly due to the reduction of data redundancy, the smoothening of the noise and irregularity and elimination of uneven point cloud density, whereas preserving key points within the dataset capable of representing the classes (Xiong et al., 2021). Though the disadvantages of grid subsampling algorithms (as the one used in this study) mainly pertains to its incapacity for preserving unevenly distributed points (Lyu et al., 2024), the dataset was acquired through aerial photogrammetry as opposed to TLS, where the point density increases closer to the sensor location. The concatenation of the three subsampled point clouds, where each subsampling is combined with each other, prior to the calculation of the features brought back the details lost in the coarser scales (Refer to section 4.4).

6.2. Height features

The values of absolute mean height per class resulted in a sporadic distribution with peaks and valleys at similar height values with different densities (Figure 10), while values of relative heights displayed a clearer shift in higher height values (Figure 11). Though absolute height displayed that ground points were distributed at low values and vegetation heights at high values, the sporadic nature is possibly due to the misclassifications where ground was confused with roof. Thus, resulting in sudden increases and decreases of density since actual roofs are located at a higher elevation than ground.

The buildings in the study area, especially the academic buildings in the center, shared similar sizes, i.e., similar relative height of roofs and facade points. Though the study area was relatively flat, the misclassification in roof and ground absolute heights could be partially because the classifier learned from mostly higher elevation points and the unseen lower elevation points had roofs that were at a similar elevation as the ground in other regions of the study area (Figure 9). Thus, relative heights alleviated the discrepancy by setting ground points as a reference plane and calculating other points' height from the ground. This method proved to result in a more moderate distribution (Figure 11) and a more accurate classification (Figure 15).

As expected, height information contain valuable input for isolating large structures such as buildings. Furthermore, isolating the ground points and creating a gapless DEM are supplementary steps that are not part of the classification model, however, the additional effort proved to be worthwhile as roof structures were clearly distinguished with less errors compared to a straightforward model.

6.3. Color features

The visible spectrum expressed in the RGB space showed that it gives little opportunities for a clear distinction between the sematic labels. Not only were the patterns similar across the color space, with the three histograms skewed to the left, but also the patterns for each band followed a similar pattern, where the ascent and descent of all labels being identical at the same rate (Figure 12). The conversion to the HSV space strongly imply that certain values were unique to certain labels (Figure 13). As seen with the hue density plot, where a peak was reserved for only medium vegetation points. Similarly, saturation showed a leftward shift of density where the descent of vegetation was also isolated. These findings could explain why most vegetation points in our study area was able to be distinguished almost flawlessly by the model. The enhanced performance of using reflectance data, especially the HSV color space, is consistent with the findings of Becker et al. (2018). The information gain from the HSV color space could be attributed to its robustness to variable light conditions (Jia et al., 2019). As most buildings and ground shared the same color, using reflectance information might have posed a hindrance when it came to isolating building features, however, there exists great potential of using the color data derived from photogrammetric images for analyzing height, crown width, and diameter-at-breast-height and age of city trees (Qiu et al., 2018).

6.4. Geometric features

Low omnivariance values for roof and ground is attributed to the isotropic nature of such points, i.e., most ground points are configured along the same horizontal plane with slight variations along the vertical axis (Weinmann et al., 2013). In contrast, higher omnivariance values of vegetation is typical due to the random spread of points across all three axes. The second peak in omnivariance also pertains to ground points (Figure 14a). It could be a result of misclassified ground points that surround the perimeter of buildings and vegetation. Meanwhile the intermediary values pertained to facades due to their planar nature similar to ground points, however, facades fluctuate along two axes, since a building's wall could be aligned with an X and Y or X and Z orientation, with little-to-no variations in the thickness of facade plane (Günen, 2022). Meanwhile, edges and corners display a distinct transition from one alignment to a perpendicular configuration, explaining the presence of high omnivariance values for roof labels.

The eigenentropy values showed a high peak for most ground and facade points at the high to intermediary values since both possess an isotropic distribution (Figure 14b). On the other hand,

vegetation canopy had its density the highest at the higher eigenentropy values since canopies typically have globular structures with little prevalent direction of variance.

The entire classification labels were skewed towards high anisotropic values, with vegetation trailing slightly behind (Figure 14c). This result indicates that facade and ground structures are linearly oriented, while vegetation, even though ranging within high values, are more volumetrically spread over than ground or facade neighborhoods. Contrary to Thomas et al. (2018), who had claimed that anisotropy is strictly equivalent to sphericity, the results of this study suggest that anisotropy could be defined as the opposite of sphericity due to their inverse distributions (Figure 14 c & g).

This study also shows that linearity is the inverse of planarity as they have mirroring density histograms, while curvature and sphericity are equivalent (Figure 14 f & g). The study area appears to be mostly homogenous in terms of linearity, planarity, curvature, and sphericity, except for vegetation. This is possibly due to the absence of dedicated class labels that could encapsulate the structures that these features were meant to capture, for instance, a class for lamp posts, traffic signs, barriers, or tree trunks. Examples of such finer class details were used by Thomas et al. (2018) as they used high-resolution TLS of French streets, while another study used architecturally complex TLS datasets of historic Italian cathedrals and abbeys to classify statues and pillars (Teruggi et al., 2020). However, the use of additional classes to discriminate the finer elements of the study area was irrelevant for this study's focus of narrowing down the features useful for building extraction.

Most notably the bimodal distribution of verticality values quantitatively explains whether the points are oriented along the Z axis or not. Theoretically, this geometric feature communicates to the model the distinction between flat and vertical planes. Practically, verticality became among the most important features for classification of the study area due to its capacity in distinguishing between facade planes from ground or roof areas (Figure 14h).

Contrary to previous literature, which attempted to classify point clouds derived from LiDAR datasets (Atik et al., 2021; Teruggi et al., 2020; Thomas et al., 2018; Weinmann et al., 2015a, 2015b), this study combined the subsampling methodology of Hackel et al. (2016) and the feature extraction approach of Becker et al (2018) to classify the photogrammetric point cloud. Consequently, the differences in acquisition techniques between photogrammetry and LiDAR could have influenced the capacity of geometric features at describing the structures. In comparison to photogrammetry, LiDAR not only better accounts for small gaps and peaks, but it also has a better capability of penetrating structures, such as the vegetation canopy (Lisein et

al., 2013). Hence the lack in volumetric information in photogrammetry could have led to the incapacity of geometric features to capture the attributes that vary in depth.

6.5. Performance of model

The overall accuracies from ALL_FEAT and NO_GROUND, was 0.94 and 0.95 respectively (Figure 15). These accuracies outperformed those reported by Atik et al. (2021), who had classified their data multiple times at different radii using a similar set of geometric features, rather than utilizing the multi-scale concatenation approach as described in this study. Moreover, the accuracies reported here were comparable to that of more advanced classification techniques such as the use of convolutional neural networks (Winiwarter & Mandlburger, 2019; Wang et al., 2021).

Furthermore, the accuracies of the model ALL_FEAT and NO_GROUND criteria had a higher overall accuracy than that of Weinmann et al. (2015b) (0.88) since they had used purely geometric features on TLS datasets. However, the model with GEO_ONLY criterion of this study recorded a lower accuracy. These results are consistent with Becker et al. (2018) who had also used photogrammetric data for benchmarking classification models. They had showed that the use of geometric features alone resulted in 50% more classification errors. As previously mentioned, the unreliable performance of geometric features could be due to limitations of photogrammetry.

The pattern of precision, recall and F1 metrics is consistent with previous literature (Atik et al., 2021; Hackel et al., 2016; Weinmann et al., 2015) and higher than that of RF models that have not implemented the multi-scale approach (Atik et al., 2021; Duran et al., 2021). Hackel et al. (2016) reported the lowest metrics for the low vegetation class, while pedestrians scored least with deep learning algorithms (Wang et al., 2021). The results in this study and previous literature both confirm that lowest accuracy metrics is mainly attributed to the insufficient amount of training data by these classes.

Building information extracted by Hackel et al. (2016) were supplemented by modified versions of contour encoding algorithms such as Shape Con-text 3D (SC3D) and Signature of Histogram of Orientations (SHOT). Though their approach resulted in higher F1 scores than using geometric features alone, the present study provides comparable F1 scores, especially for roof and facade structures once all features were fully utilized (Figure 16).

The findings of this research resulted in an exceptionally good performance of COL_HEI criterion, this could be indicative of a certain degree of overfitting as most structures in the study area shared a similarity in height and color. Similarly, the dependency on color and

geometric features could suggest an explanation of the confusion between parking and roof as they share similarities in verticality and reflectance values in the study area tile (Figure 18).
While the accuracy metrics indicate that geometric features on their own performed poorly, the integration of geometric features in combination with either color or vegetation features provided higher F1 scores. Features such as omnivariance and verticality showed isolated peaks unique to roof and facade structures explaining their role in enhancing the classification.
Contrary to Kumar et al.'s (2019) findings, vegetation classes did not pose a major problem as they were primarily not confused with building roof or facade structures. However, the sub classes of vegetation (low, medium, and high) seemed to be not well distinguished from each other. The issue is especially apparent with the NO_GROUND criterion since most of the medium vegetation was classified as high vegetation. This could be due to anomalies in the manual classification or a relative height computation error. Nonetheless, since the model was capable of separating most vegetation points from non-vegetation points, a grouping of the three vegetation classes into one, as suggested by Pessoa et al. (2019), could alleviate the issue.
Despite the high accuracy level of ALL_FEAT and NO_GROUND, the qualitative analysis revealed macroscopic classification errors sustained throughout the study area. Such errors could be the result of label imbalances within the reference point cloud, overfitting of the RF model, or reference data distribution lacking proper representation of the study area.
While this study's grid search resulted in hyper-parameters that are similar to those reported by other authors (Becker et al., 2018; Duran et al., 2021; Hackel et al., 2016), their training and predicting steps registered between 1 and 50 seconds, which was vastly shorter than this study's computation times under identical computational resources (Refer to section 4.6). This is firstly due to the difference in point count for each class, for instance, Duran et al. (2021) using 100,000 points per label or Becker et al.(2018) randomly supplying 1000 points for each label. Secondly, the authors utilized FLANN for neighborhood querying. FLANN is considered to be much faster than the Python packages used in this study since libraries written in C++ are more efficient than Python at memory consumption and utilization timings for searching algorithms (Zehra et al., 2020).

6.6. Validation

Studies that developed the method used benchmark datasets such as Paris-Rue-Madame (Hackel et al., 2016), Paris-Rue-Cassette (Weinmann et al., 2015b), Stanford Large-Scale 3D Indoor Spaces Dataset (Thomas et al., 2018), Oakland3D and the Vaihingen TLS (Atik et al., 2021). Benchmark datasets already possess classification labels which could be used to validate

the output of the model being developed. However, when the intention is to classify self-acquired datasets, the validation proves to be difficult since pre-classified datasets with low geometric uncertainties are likely to not exist. Hence performance metrics are exclusively used to evaluate the model (Duran et al., 2021). Despite these limitations, the grid of points, which was used to validate the consistency of roof points classified by the RF model with the PICC dataset, proved to be a meaningful and reproducible method to measure the accuracy of alignment of rooftops. This is due to the increasing effort for standardization and accessibility of geographic datasets, equivalent to PICC, globally and especially within the European Union (Bartha & Kocsis, 2022).

Moreover, the validation method reveals that even though the model scored high performance metrics, around a quarter of the dataset of roof points was misclassified (Figure 23). It is evident that the misclassified points represented, among other points, mostly ground points which were remnants from the CSF (Figure 24a). Hence, the confusion between roof and ground points remained but to a lesser extent. Relative height calculation facilitated in applying a global height threshold across the study area that would not be conflated with elevations, since, as previously mentioned, some grounds could share similar elevations as roofs (Figure 24b).

6.7. Limitations

Several limitations arise with this method of classification starting with the very first step. The model relies on a reference point cloud. Manual classification could not be perfect due to the messy nature of point clouds, which might possess several ambiguous points that the user could fully interpret.

The computation effort that is needed for processing each point and querying for its neighborhood before performing matrix calculations is immense and could not be done on personal computers when large study areas are considered. Furthermore, Python programming language adds an additional complexity to the computation efficiency problem. Therefore, low-level computer languages should be chosen if the goal is to classify at the scale of the entire city.

Though geometric features provide valuable information for feature extraction, they need to be combined with other features for a robust classification. Moreover, it should be reminded that photogrammetric data does not have the volumetric information required to extract features with more depth, thus the capacity of geometric features is at times further hindered. While high scores and performance metrics are reported, the actual margin of classification error is much larger and could not be validated since validation is difficult as classified datasets of the

same resolution is absent. This method delivers a starting point for further analyses by providing a segmented and classified point cloud, however, qualitative human interpretation of the result along with manual reclassification is still required.

Additionally, even if the facade was correctly classified, photogrammetric 3D point clouds result in gaps in the data due to different reflective properties. Thus, applications that would require the total area of facades in a landscape should consider interpolation algorithms to fill the data gaps. Otherwise, it would be more advantageous to utilize different acquisition techniques for a more detailed representation of buildings.

6.8. Recommendations

If, as the present study suggests, the model tends to classify structures based on similar elevation, color, or geometric data, then there is a need for enhancing the model by training and testing it on different areas across Louvain-la-Neuve to avoid overfitting. Moreover, different scales and number of scales should be explored to find a better suitable for the features of the city. Although vegetation was not perfectly divided into low, medium, and high, it was still well defined from the other structures, thus, the implementation of this technique with other applications such as city tree quantification, carbon stock calculation or biomass estimation could be worth investigating.

It is also important to develop a post-processing algorithm that has the capability of filtering out misclassified points by identifying whether the points belong to a cluster of a similar class or not rather than relying on low relative height values alone.

In terms of future analyses, it would be useful to extend the current findings by developing a pipeline for the post-processing clean up algorithm and creating a CityGML model from the classified data. Furthermore, the utilized geometric features within this study should provide insight into the features that could be discarded in future classification attempts since some possessed either similar or opposite distributions such as curvature and sphericity or planarity and linearity.

The proposed semantic classification methodology should serve as stepping-stone for creating a 3D model and initiate the road towards establishing a fully-functional digital twin of Louvain-la-Neuve.

Chapter 7. Conclusion

This study aimed to kick-start the process of creating a city 3D model for Louvain-la-Neuve by exploring a supervised classification technique for a photogrammetric point cloud dataset. The classification algorithm was trained on geometric features enriched with height and reflectance values. To augment the discriminative power, a multi-scale point-wise classification approach was adopted. It was found that geometric features, although undescriptive alone, provided considerable improvements to classification metrics when combined with the other descriptors. In the context of extracting buildings some features such as verticality, height and omnivariance stood out more than others. Furthermore, additional steps in the workflow such as iterative subsampling, relative height computation and conversion of color values to the HSV domain proved to contribute positively for the extraction of vegetation and built-up structures. Such steps reduced inter-class confusion between ground and roof classes while gaining the capacity to distinguish vegetation points from others.

The establishment of semantic classification pipeline paves the way for creating a city 3D model. This can aid in the modelling of natural disasters, estimating the demand of energy, and informing urban planners to promote greener and healthier cities. By focusing on building extraction and pinpointing influential descriptive features, future research and projects could use the proposed methodology and workflow as a blueprint for classifying the rest of the point cloud tiles. Moreover, the methodology performed either comparably or better at machine learning performance metrics when compared to previous scientific works that had used similar techniques.

Given that each point was queried individually to find its neighboring points, the repetitive subsampling of the point cloud showed to be one of the most important steps in the workflow as it dramatically decreased point density while preserving geometries. Moreover, the use of multiple scales proved to bring back any data that might have been lost at the coarsest subsampling scale. Hence subsampling the point cloud is a major advancement to the point-wise classification technique and benefits heavily for dealing with voluminous point cloud datasets as it reduces redundancy and maintains structural integrity. Thus, voxel-grid filter subsampling algorithm should be considered projects that involve point-wise iteration procedures.

The use of geometric features as the sole descriptor of the scene performed the worst by receiving the lowest performance scores on all accounts, however, their combination with either height or color or both proved to enhance accuracies for facade and roof extraction. Furthermore, the extraction of vegetation proved to be excellent due to valuable reflectance

information derived from photogrammetry. Thus, further applications in urban greenery could have a starting point from this classification technique.

The limitations of the classification model were highlighted using visual interpretation and a validation of the model's output using PICC dataset. Validation was limited to just roof points, where the accuracy increased from 75% to 91% due to applying a global threshold based on relative heights. Underlining the importance for implementing additional post-processing algorithms or manual data cleaning steps in the workflow to obtain a more accurate end-product.

This study demonstrated the ability of classifying a point cloud and extracting valuable semantic information for city 3D models, however, the processing, training, and predicting times consumed multiple hours for a single tile. Thus, to have a point cloud at the scale of the whole city classified, the efficiency of the workflow must be increased. It was proposed to convert to low-level languages to evade slow run-times that plagued Python.

Bibliography

Agisoft. (2024). Agisoft Metashape [Computer software]. https://www.agisoft.com/

Ajjur, S. B., & Al-Ghamdi, S. G. (2022). Exploring urban growth–climate change–flood risk nexus in fast growing cities. Scientific Reports, 12(1), 12265. https://doi.org/10.1038/s41598-022-16475-x

Al-Ghamdi, K. A., Elzahrany, R. A., Mirza, M. N., & Dawod, G. M. (2012). Impacts of urban growth on flood hazards in Makkah City, Saudi Arabia. International Journal of Water Resources and Environmental Engineering, 4(2), 23–34.

Alidoost, F., & Arefi, H. (2017). COMPARISON OF UAS-BASED PHOTOGRAMMETRY SOFTWARE FOR 3D POINT CLOUD GENERATION: A SURVEY OVER A HISTORICAL SITE. ISPRS Annals of the Photogrammetry, Remote Sensing and Spatial Information Sciences, IV-4/W4, 55–61. https://doi.org/10.5194/isprs-annals-IV-4-W4-55-2017

Arya, S., Mount, D. M., Netanyahu, N. S., Silverman, R., & Wu, A. Y. (1998). An optimal algorithm for approximate nearest neighbor searching fixed dimensions. Journal of the ACM, 45(6), 891–923. https://doi.org/10.1145/293347.293348

Atik, M. E., Duran, Z., & Seker, D. Z. (2021). Machine Learning-Based Supervised Classification of Point Clouds Using Multiscale Geometric Features. ISPRS International Journal of Geo-Information, 10(3), 187. https://doi.org/10.3390/ijgi10030187

Azevedo Guedes, A., Carvalho Alvarenga, J., Dos Santos Sgarbi Goulart, M., Rodriguez Y Rodriguez, M., & Pereira Soares, C. (2018). Smart Cities: The Main Drivers for Increasing the Intelligence of Cities. Sustainability, 10(9), 3121. https://doi.org/10.3390/su10093121

Baltsavias, E. P. (1999). A comparison between photogrammetry and laser scanning. ISPRS Journal of Photogrammetry and Remote Sensing, 54(2–3), 83–94.

Bartha, G., & Kocsis, S. (2022). STANDARDIZATION OF GEOGRAPHIC DATA: THE EUROPEAN INSPIRE DIRECTIVE. European Journal of Geography, 2(2). https://eurogeojournal.eu/index.php/egj/article/view/36

Batty, M. (2014). Can it happen again? Planning support, Lee's Requiem and the rise of the smart cities movement. Environment and Planning B: Planning and Design, 41(3), 388–391.

Becker, C., Rosinskaya, E., Häni, N., D'Angelo, E., & Strecha, C. (2018). Classification of Aerial Photogrammetric 3D Point Clouds. Photogrammetric Engineering & Remote Sensing, 84(5), 287–295. https://doi.org/10.14358/PERS.84.5.287

Bekkar, A., Hssina, B., Douzi, S., & Douzi, K. (2021). Air-pollution prediction in smart city, deep learning approach. Journal of Big Data, 8(1), 161. https://doi.org/10.1186/s40537-021-00548-1

Bera, B., Chinta, S., Mahajan, D., Sailaja, A., & Mahajan, R. (2023). Urbanization and Its Impact on Environmental Sustainability: A Comprehensive Review. Harbin Gongcheng Daxue Xuebao/Journal of Harbin Engineering University, 44, 1310–1318.

Biljecki, F., Stoter, J., Ledoux, H., Zlatanova, S., & Çöltekin, A. (2015). Applications of 3D City Models: State of the Art Review. ISPRS International Journal of Geo-Information, 4(4), 2842–2889. https://doi.org/10.3390/ijgi4042842

Bornaz, L., Rinaudo, F., & others. (2004). Terrestrial laser scanner data processing. XXth ISPRS Congress Istanbul.

Breiman, L. (2001). Machine Learning. 45(1), 5–32. https://doi.org/10.1023/A:1010933404324

Bremer, M., Mayr, A., Wichmann, V., Schmidtner, K., & Rutzinger, M. (2016). A new multi-scale 3D-GIS-approach for the assessment and dissemination of solar income of digital city models. Computers, Environment and Urban Systems, 57, 144–154. https://doi.org/10.1016/j.compenvurbsys.2016.02.007

Brodu, N., & Lague, D. (2012). 3D terrestrial lidar data classification of complex natural scenes using a multi-scale dimensionality criterion: Applications in geomorphology. ISPRS Journal of Photogrammetry and Remote Sensing, 68, 121–134.

Butler, H., Chambers, B., Hartzell, P., & Glennie, C. (2021). PDAL: An open source library for the processing and analysis of point clouds. Computers & Geosciences, 148, 104680. https://doi.org/10.1016/j.cageo.2020.104680

Cavallo, M. (2015). 3d city reconstruction from google street view. Comput. Graph. J.

Charlier, J. (1977). Louvain-la-Neuve, Belgium, from campus to new town. GeoJournal, 1(4), 47–55. https://doi.org/10.1007/BF00845202

Chen, R. (2011). The development of 3D city model and its applications in urban planning. 2011 19th International Conference on Geoinformatics, 1–5. https://doi.org/10.1109/GeoInformatics.2011.5981007

Chen, Z., Yu, B., Li, Y., Wu, Q., Wu, B., Huang, Y., Wu, S., Yu, S., Mao, W., Zhao, F., & Wu, J. (2022). Assessing the potential and utilization of solar energy at the building-scale in

Shanghai. Sustainable Cities and Society, 82, 103917. https://doi.org/10.1016/j.scs.2022.103917

Cho, Y. H., & Kim, Y. (1983). The challenge of urban overpopulation and public policy: The case of metropolitan Seoul. Journal of East and West Studies, 12(2), 23–49. https://doi.org/10.1080/12265088308422705

Colding, J., Colding, M., & Barthel, S. (2020). The smart city model: A new panacea for urban sustainability or unmanageable complexity? Environment and Planning B: Urban Analytics and City Science, 47(1), 179–187. https://doi.org/10.1177/2399808318763164

Collis, R. (1970). Lidar. Applied Optics, 9(8), 1782–1788.

Deng, T., Zhang, K., & Shen, Z.-J. (Max). (2021). A systematic review of a digital twin city: A new pattern of urban governance toward smart cities. Journal of Management Science and Engineering, 6(2), 125–134. https://doi.org/10.1016/j.jmse.2021.03.003

Duran, Z., Ozcan, K., & Atik, M. E. (2021). Classification of Photogrammetric and Airborne LiDAR Point Clouds Using Machine Learning Algorithms. Drones, 5(4), 104. https://doi.org/10.3390/drones5040104

El-Sayed, E., Abdel-Kader, R. F., Nashaat, H., & Marei, M. (2018). Plane detection in 3D point cloud using octree-balanced density down-sampling and iterative adaptive plane extraction. IET Image Processing, 12(9), 1595–1605. https://doi.org/10.1049/iet-ipr.2017.1076

Feng, C.-C., & Guo, Z. (2021). A Hierarchical Approach for Point Cloud Classification With 3D Contextual Features. IEEE Journal of Selected Topics in Applied Earth Observations and Remote Sensing, 14, 5036–5048. https://doi.org/10.1109/JSTARS.2021.3077568

Follmann, A., Willkomm, M., & Dannenberg, P. (2021). As the city grows, what do farmers do? A systematic review of urban and peri-urban agriculture under rapid urban growth across the Global South. Landscape and Urban Planning, 215, 104186. https://doi.org/10.1016/j.landurbplan.2021.104186

Friedman, J. H., Bentley, J. L., & Finkel, R. A. (1977). An algorithm for finding best matches in logarithmic expected time. ACM Transactions on Mathematical Software (TOMS), 3(3), 209–226.

Girardeau-Montaut, D. (2014). CloudCompare (Version 2.13) [Computer software]. www.cloudcompare.org

Graham, L. (2015). The LAS 1.4 Specification. ASPRS Lidar Division. https://www.asprs.org/wp-content/uploads/2010/12/LAS_Specification.pdf

Grilli, E., Menna, F., & Remondino, F. (2017). A REVIEW OFPOINT CLOUDS SEGMENTATION AND CLASSIFICATION ALGORITHMS. The International Archives of the Photogrammetry, Remote Sensing and Spatial Information Sciences, XLII-2/W3, 339–344. https://doi.org/10.5194/isprs-archives-XLII-2-W3-339-2017

Günen, M. A. (2022). Adaptive neighborhood size and effective geometric features selection for 3D scattered point cloud classification. Applied Soft Computing, 115, 108196. https://doi.org/10.1016/j.asoc.2021.108196

Hackel, T., Wegner, J. D., & Schindler, K. (2016). FAST SEMANTIC SEGMENTATION OF 3D POINT CLOUDS WITH STRONGLY VARYING DENSITY. ISPRS Annals of the Photogrammetry, Remote Sensing and Spatial Information Sciences, III–3, 177–184. https://doi.org/10.5194/isprs-annals-III-3-177-2016

Howland, M. D., Tamberino, A., Liritzis, I., & Levy, T. E. (2022). Digital Deforestation: Comparing Automated Approaches to the Production of Digital Terrain Models (DTMs) in Agisoft Metashape. Quaternary, 5(1), 5. https://doi.org/10.3390/quat5010005

Huang, R., Hong, D., Xu, Y., Yao, W., & Stilla, U. (2020). Multi-Scale Local Context Embedding for LiDAR Point Cloud Classification. IEEE Geoscience and Remote Sensing Letters, 17(4), 721–725. https://doi.org/10.1109/LGRS.2019.2927779

Huang, Y., Chen, Z., Wu, B., Chen, L., Mao, W., Zhao, F., Wu, J., Wu, J., & Yu, B. (2015). Estimating Roof Solar Energy Potential in the Downtown Area Using a GPU-Accelerated Solar Radiation Model and Airborne LiDAR Data. Remote Sensing, 7(12), 17212–17233. https://doi.org/10.3390/rs71215877

Isa, S. M., Shukor, S. A., Rahim, N., Maarof, I., Yahya, Z., Zakaria, A., Abdullah, A., & Wong, R. (2018). A review of data structure and filtering in handling 3D big point cloud data for building preservation. 2018 IEEE Conference on Systems, Process and Control (ICSPC), 141–146.

Islam, M., & Reza, S. (2019). The rise of big data and cloud computing. Internet Things Cloud Comput, 7(2), 45.

James, F. J., Romine, J. A., & Zwanzig, P. E. (1998). The effects of immigration on urban communities. Cityscape, 171–192.

Jia, C., Yang, T., Wang, C., Fan, B., & He, F. (2019). A new fast filtering algorithm for a 3D point cloud based on RGB-D information. PLOS ONE, 14(8), e0220253. https://doi.org/10.1371/journal.pone.0220253

Jutzi, B., & Gross, H. (2009). Nearest neighbour classification on laser point clouds to gain object structures from buildings. The International Archives of the Photogrammetry, Remote Sensing and Spatial Information Sciences, 38(Part 1), 4–7.

Kaden, R., & Kolbe, T. H. (2013). City-wide total energy demand estimation of buildings using semantic 3D city models and statistical data. ISPRS Annals of the Photogrammetry, Remote Sensing and Spatial Information Sciences, 2, 163–171.

Kolečanský, Š., Hofierka, J., Bogľarský, J., & Šupinský, J. (2021). Comparing 2D and 3D Solar Radiation Modeling in Urban Areas. Energies, 14(24), 8364. https://doi.org/10.3390/en14248364

Kumar, A., Anders, K., Winiwarter, L., & Höfle, B. (2019). FEATURE RELEVANCE ANALYSIS FOR 3D POINT CLOUD CLASSIFICATION USING DEEP LEARNING. ISPRS Annals of the Photogrammetry, Remote Sensing and Spatial Information Sciences, IV-2/W5, 373–380. https://doi.org/10.5194/isprs-annals-IV-2-W5-373-2019

Kurakula, V., Skidmore, A., Kluijver, H., Stoter, J., Dabrowska Zielinska, K., & Kuffer, M. (2007). A GIS based approach for 3D noise modelling using 3D city models.

Lafortune, G., Zoeteman, K., Fuller, G., Mulder, R., Dagevos, J., & Schmidt-Traub, G. (2019). The 2019 SDG Index and Dashboards Report for European Cities (prototype version). Sustainable Development Solutions Network (SDSN) and the Brabant Center for Sustainable Development (Telos). https://www.sustainabledevelopment.report/reports/sdg-index-and-dashboards-report-for-european-cities/

León-Sánchez, C., Giannelli, D., Agugiaro, G., & Stoter, J. (2021). Testing the new 3D bag dataset for energy demand estimation of residential buildings. The International Archives of the Photogrammetry, Remote Sensing and Spatial Information Sciences, 46, 69–76.

Lisein, J., Pierrot-Deseilligny, M., Bonnet, S., & Lejeune, P. (2013). A Photogrammetric Workflow for the Creation of a Forest Canopy Height Model from Small Unmanned Aerial System Imagery. Forests, 4(4), 922–944. https://doi.org/10.3390/f4040922

Liu, Y., Huang, B., Guo, H., & Liu, J. (2023). A big data approach to assess progress towards Sustainable Development Goals for cities of varying sizes. Communications Earth & Environment, 4(1), 66. https://doi.org/10.1038/s43247-023-00730-8

Lu, L., Becker, T., & Löwner, M.-O. (2017). 3D Complete Traffic Noise Analysis Based on CityGML. In A. Abdul-Rahman (Ed.), Advances in 3D Geoinformation (pp. 265–283). Springer International Publishing. https://doi.org/10.1007/978-3-319-25691-7_15

Lyu, W., Ke, W., Sheng, H., Ma, X., & Zhang, H. (2024). Dynamic Downsampling Algorithm for 3D Point Cloud Map Based on Voxel Filtering. Applied Sciences, 14(8), 3160. https://doi.org/10.3390/app14083160

Madlener, R., & Sunak, Y. (2011). Impacts of urbanization on urban structures and energy demand: What can we learn for urban energy planning and urbanization management? Sustainable Cities and Society, 1(1), 45–53. https://doi.org/10.1016/j.scs.2010.08.006

Minařík, R., & Langhammer, J. (2016). USE OF A MULTISPECTRAL UAV PHOTOGRAMMETRY FOR DETECTION AND TRACKING OF FOREST DISTURBANCE DYNAMICS. The International Archives of the Photogrammetry, Remote Sensing and Spatial Information Sciences, XLI-B8, 711–718. https://doi.org/10.5194/isprs-archives-XLI-B8-711-2016

Muja, M., & Lowe, D. (2009). Flann-fast library for approximate nearest neighbors user manual. Computer Science Department, University of British Columbia, Vancouver, BC, Canada, 5, 6.

Murshed, S. M., Picard, S., & Koch, A. (2018). Modelling, Validation and Quantification of Climate and Other Sensitivities of Building Energy Model on 3D City Models. ISPRS International Journal of Geo-Information, 7(11), 447.

Niemeyer, J., Rottensteiner, F., & Soergel, U. (2014). Contextual classification of lidar data and building object detection in urban areas. ISPRS Journal of Photogrammetry and Remote Sensing, 87, 152–165. https://doi.org/10.1016/j.isprsjprs.2013.11.001

Nouvel, R., Schulte, C., Eicker, U., Pietruschka, D., & Coors, V. (2013). CityGML-based 3D city model for energy diagnostics and urban energy policy support. Building Simulation 2013, 13, 218–225.

Ntuli, S., & Forbes, A. (2023). Classification of 3D UAS-SfM Point Clouds in the Urban Environment. South African Journal of Geomatics, 12(2), 190–205.

Pedregosa, F., Varoquaux, G., Gramfort, A., Michel, V., Thirion, B., Grisel, O., Blondel, M., Prettenhofer, P., Weiss, R., Dubourg, V., & others. (2011). Scikit-learn: Machine learning in Python. The Journal of Machine Learning Research, 12, 2825–2830.

Pérez, M., Agüera, F., & Carvajal, F. (2013). LOW COST SURVEYING USING AN UNMANNED AERIAL VEHICLE. The International Archives of the Photogrammetry, Remote Sensing and Spatial Information Sciences, XL-1/W2, 311–315. https://doi.org/10.5194/isprsarchives-XL-1-W2-311-2013

Pessoa, G. G., Amorim, A., Galo, M., & Galo, M. D. L. B. T. (2019). PHOTOGRAMMETRIC POINT CLOUD CLASSIFICATION BASED ON GEOMETRIC AND

RADIOMETRIC DATA INTEGRATION. Boletim de Ciências Geodésicas, 25(spe), e2019S001. https://doi.org/10.1590/s1982-21702019000s00001

PICC. (2024). PICC: La référence cartographique de la Wallonie [Dataset]. https://geoportail.wallonie.be/georeferentiel/PICC

Pix4D. (2024). Pix4D [Computer software]. https://www.pix4d.com/

Pradhan, P., Costa, L., Rybski, D., Lucht, W., & Kropp, J. P. (2017). A Systematic Study of Sustainable Development Goal (SDG) Interactions. Earth's Future, 5(11), 1169–1179. https://doi.org/10.1002/2017EF000632

QGIS developers. (2024). Fill NoData algorithm. QGIS Documentation. https://docs.qgis.org/testing/en/docs/user_manual/processing_algs/gdal/rasteranalysis.html#fill-nodata

Qiu, Z., Feng, Z.-K., Wang, M., Li, Z., & Lu, C. (2018). Application of UAV Photogrammetric System for Monitoring Ancient Tree Communities in Beijing. Forests, 9(12), 735. https://doi.org/10.3390/f9120735

Rabbani, T., Van Den Heuvel, F., & Vosselmann, G. (2006). Segmentation of point clouds using smoothness constraint. International Archives of Photogrammetry, Remote Sensing and Spatial Information Sciences, 36(5), 248–253.

Rao, Y., Yang, J., Dai, D., Wu, K., & He, Q. (2021). Urban growth pattern and commuting efficiency: Empirical evidence from 100 Chinese cities. Journal of Cleaner Production, 302, 126994. https://doi.org/10.1016/j.jclepro.2021.126994

Ridzuan, N., Ujang, U., & Azri, S. (2023). 3D vectorization and rasterization of CityGML standard in wind simulation. Earth Science Informatics, 16(3), 2635–2647. https://doi.org/10.1007/s12145-023-01065-w

Ridzuan, N., Ujang, U., Azri, S., & Yusoff, I. M. (2022). Computational Fluid Dynamics of Wind Flow and Air Pollution Modelling: A Review on 3D Building Model Standards. IOP Conference Series: Earth and Environmental Science, 1064(1), 012051. https://doi.org/10.1088/1755-1315/1064/1/012051

Romero Rodríguez, L., Duminil, E., Sánchez Ramos, J., & Eicker, U. (2017). Assessment of the photovoltaic potential at urban level based on 3D city models: A case study and new methodological approach. Solar Energy, 146, 264–275. https://doi.org/10.1016/j.solener.2017.02.043

Sahin, C., Alkis, A., Ergun, B., Kulur, S., Batuk, F., & Kilic, A. (2012). Producing 3D city model with the combined photogrammetric and laser scanner data in the example of

Taksim Cumhuriyet square. Optics and Lasers in Engineering, 50(12), 1844–1853. https://doi.org/10.1016/j.optlaseng.2012.05.019

Saleri, R., Cappellini, V., Nony, N., De Luca, L., Pierrot-Deseilligny, M., Bardiere, E., & Campi, M. (2013). UAV photogrammetry for archaeological survey: The Theaters area of Pompeii. 2013 Digital Heritage International Congress (DigitalHeritage), 497–502. https://doi.org/10.1109/DigitalHeritage.2013.6744818

Sarzynski, A. (2012). Bigger Is Not Always Better: A Comparative Analysis of Cities and their Air Pollution Impact. Urban Studies, 49(14), 3121–3138. https://doi.org/10.1177/0042098011432557

Schenk, T. (2005). Introduction to photogrammetry. The Ohio State University, Columbus, 106(1).

Schröter, K., Lüdtke, S., Redweik, R., Meier, J., Bochow, M., Ross, L., Nagel, C., & Kreibich, H. (2018). Flood loss estimation using 3D city models and remote sensing data. Environmental Modelling & Software, 105, 118–131. https://doi.org/10.1016/j.envsoft.2018.03.032

Schrotter, G., & Hürzeler, C. (2020). The digital twin of the city of Zurich for urban planning. PFG–Journal of Photogrammetry, Remote Sensing and Geoinformation Science, 88(1), 99–112.

Shoab, M., Singh, V. K., & Ravibabu, M. V. (2022). High-Precise True Digital Orthoimage Generation and Accuracy Assessment based on UAV Images. Journal of the Indian Society of Remote Sensing, 50(4), 613–622. https://doi.org/10.1007/s12524-021-01364-z

Stéphenne, N., Beaumont, B., Veschkens, M., Palm, S., & Charlemagne, C. (2015). Spatial Data Uncertainty in a Webgis Tool Supporting Sediments Management in Wallonia. The International Archives of the Photogrammetry, Remote Sensing and Spatial Information Sciences, 40, 625–628.

Stoter, J., Arroyo Ohori, K., Dukai, B., Labetski, A., Kumar, K., Vitalis, S., & Ledoux, H. (2020). State of the Art in 3D City Modelling: Six Challenges Facing 3D Data as a Platform. GIM International: The Worldwide Magazine for Geomatics, 34. https://www.gim-international.com/content/article/state-of-the-art-in-3d-city-modelling-2

Stoter, J., De Kluijver, H., & Kurakula, V. (2008). 3D noise mapping in urban areas. International Journal of Geographical Information Science, 22(8), 907–924. https://doi.org/10.1080/13658810701739039

Strzalka, A., Bogdahn, J., Coors, V., & Eicker, U. (2011). 3D City modeling for urban scale heating energy demand forecasting. HVAC&R Research, 17(4), 526–539.

Suomalainen, K., Wang, V., & Sharp, B. (2017). Rooftop solar potential based on LiDAR data: Bottom-up assessment at neighbourhood level. Renewable Energy, 111, 463–475. https://doi.org/10.1016/j.renene.2017.04.025

Sushinsky, J. R., Rhodes, J. R., Possingham, H. P., Gill, T. K., & Fuller, R. A. (2013). How should we grow cities to minimize their biodiversity impacts? Global Change Biology, 19(2), 401–410.

Teruggi, S., Grilli, E., Russo, M., Fassi, F., & Remondino, F. (2020). A Hierarchical Machine Learning Approach for Multi-Level and Multi-Resolution 3D Point Cloud Classification. Remote Sensing, 12(16), 2598. https://doi.org/10.3390/rs12162598

Thomas, H., Goulette, F., Deschaud, J.-E., Marcotegui, B., & LeGall, Y. (2018). Semantic Classification of 3D Point Clouds with Multiscale Spherical Neighborhoods. 2018 International Conference on 3D Vision (3DV), 390–398. https://doi.org/10.1109/3DV.2018.00052

Tong, H., & Kang, J. (2021). Relationship between urban development patterns and noise complaints in England. Environment and Planning B: Urban Analytics and City Science, 48(6), 1632–1649.

Tsouros, D. C., Bibi, S., & Sarigiannidis, P. G. (2019). A Review on UAV-Based Applications for Precision Agriculture. Information, 10(11), 349. https://doi.org/10.3390/info10110349

Ujang, U. (2015). An amalgamation of 3D city models in urban air quality modelling for improving visual impact analysis (F. Anton, A. Ariffin, D. Mioc, & S. Azri, Eds.; pp. 51–61). https://doi.org/10.2495/AIR150051

UN DESA. (2022). World Population Prospects 2022: Summary of Results (Sales No. E.22.XIII.3). United Nations publication.

University of Tartu. (2018). UT Rocket. share.neic.no. https://doi.org/10.23673/PH6N-0144

Verma, V., Kumar, R., & Hsu, S. (2006). 3D building detection and modeling from aerial LIDAR data. 2006 IEEE Computer Society Conference on Computer Vision and Pattern Recognition (CVPR'06), 2, 2213–2220.

Wang, Y., Wang, J., Chang, S., Sun, L., An, L., Chen, Y., & Xu, J. (2021). Classification of Street Tree Species Using UAV Tilt Photogrammetry. Remote Sensing, 13(2), 216. https://doi.org/10.3390/rs13020216

Wani, M. A., & Arabnia, H. R. (2003). Parallel edge-region-based segmentation algorithm targeted at reconfigurable multiring network. The Journal of Supercomputing, 25, 43–62.

Waqas, H., Jiang, Y., Shang, J., Munir, I., & Khan, F. U. (2023). An Integrated Approach for 3D Solar Potential Assessment at the City Scale. Remote Sensing, 15(23), 5616. https://doi.org/10.3390/rs15235616

Weinmann, M., Jutzi, B., Hinz, S., & Mallet, C. (2015a). Semantic point cloud interpretation based on optimal neighborhoods, relevant features and efficient classifiers. ISPRS Journal of Photogrammetry and Remote Sensing, 105, 286–304. https://doi.org/10.1016/j.isprsjprs.2015.01.016

Weinmann, M., Jutzi, B., & Mallet, C. (2013). Feature relevance assessment for the semantic interpretation of 3D point cloud data. ISPRS Annals of the Photogrammetry, Remote Sensing and Spatial Information Sciences, II-5/W2, 313–318. https://doi.org/10.5194/isprsannals-II-5-W2-313-2013

Weinmann, M., Urban, S., Hinz, S., Jutzi, B., & Mallet, C. (2015b). Distinctive 2D and 3D features for automated large-scale scene analysis in urban areas. Computers & Graphics, 49, 47–57. https://doi.org/10.1016/j.cag.2015.01.006

West, K. F., Webb, B. N., Lersch, J. R., Pothier, S., Triscari, J. M., & Iverson, A. E. (2004). Context-driven automated target detection in 3D data (F. A. Sadjadi, Ed.; pp. 133–143). https://doi.org/10.1117/12.542536

Westoby, M. J., Brasington, J., Glasser, N. F., Hambrey, M. J., & Reynolds, J. M. (2012). 'Structure-from-Motion' photogrammetry: A low-cost, effective tool for geoscience applications. Geomorphology, 179, 300–314. https://doi.org/10.1016/j.geomorph.2012.08.021

Willenborg, B., Sindram, M., & Kolbe, T. H. (2018). Applications of 3D City Models for a Better Understanding of the Built Environment. In M. Behnisch & G. Meinel (Eds.), Trends in Spatial Analysis and Modelling: Decision-Support and Planning Strategies (Vol. 19, pp. 167–191). Springer International Publishing. https://doi.org/10.1007/978-3-319-52522-8

Winiwarter, L., & Mandlburger, G. (2019). Classification of 3D point clouds using deep neural networks. Proc. Dreiländertagung Der DGPF, Der OVG Und Der SGPF in Vienna, 28, 663–674.

Xiangfeng Liu, Peng Chen, Xiaohua Tong, Shuang Liu, Shijie Liu, Zhonghua Hong, Lingyun Li, & Kuifeng Luan. (2012). UAV-based low-altitude aerial photogrammetric

application in mine areas measurement. 2012 Second International Workshop on Earth Observation and Remote Sensing Applications, 240–242. https://doi.org/10.1109/EORSA.2012.6261173

Xiong, B., Jiang, W., Li, D., & Qi, M. (2021). Voxel Grid-Based Fast Registration of Terrestrial Point Cloud. Remote Sensing, 13(10), 1905. https://doi.org/10.3390/rs13101905

Xue, F., Lu, W., Chen, Z., & Webster, C. J. (2020). From LiDAR point cloud towards digital twin city: Clustering city objects based on Gestalt principles. ISPRS Journal of Photogrammetry and Remote Sensing, 167, 418–431. https://doi.org/10.1016/j.isprsjprs.2020.07.020

Yin, C., Xiong, Z., Chen, H., Wang, J., Cooper, D., & David, B. (2015). A literature survey on smart cities. Science China. Information Sciences, 58(10), 1–18.

Zehra, F., Javed, M., Khan, D., & Pasha, M. (2020). Comparative Analysis of C++ and Python in Terms of Memory and Time. https://doi.org/10.20944/preprints202012.0516.v1

Zhang, W., Qi, J., Wan, P., Wang, H., Xie, D., Wang, X., & Yan, G. (2016). An Easy-to-Use Airborne LiDAR Data Filtering Method Based on Cloth Simulation. Remote Sensing, 8(6), 501. https://doi.org/10.3390/rs8060501

Zhao, W.-J., Liu, E., Gao, S., Poh, H. J., KelvinWenhui, L. I., & Tan, S. T. (2016). Traffic noise prediction and mapping with virtual 3 D city models. https://api.semanticscholar.org/CorpusID:13818083

Zheng, Z., Wang, C., Zha, B., Liu, H., & Zhang, H. (2024). Fast subsampling strategy for point cloud based on novel octree coding. Measurement Science and Technology, 35(4), 045028.

Appendix

Table A1. Feature calculation times (in minutes) for each radius including computing relative heights and relative height statistics for each point in the neighborhood.

Feature	Radius 1	Radius 2	Radius 3	Total time (min)
Geometric	46.86	16.61	4.70	68.17
Absolute height	18.13	6.49	1.86	26.47
Relative height	4319.52	1927.58	581.16	6828.26
Color	16.22	6.11	1.75	24.08
Total time (min)	4400.72	1956.78	589.47	6946.98

Table A2. Confusion matrix based on the ALL_FEAT criterion.

		Predicted class						
		Ground	Low Vegetation	Medium Vegetation	High Vegetation	Roof	Facade	Vehicle
Actual class	Ground	694294	6783	6622	0	3038	7616	692
	Low Vegetation	15996	143511	32345	0	588	4708	141
	Medium Vegetation	14741	6622	1094825	1197	1651	7614	139
	High Vegetation	37	8	22434	21303	21	49	34
	Roof	16242	1348	2745	6	562008	18254	409
	Facade	5842	2845	6337	5	13120	662200	174
	Vehicle	3218	522	821	0	1026	1839	22497

Table A3. Tabulated F1 Scores.

Criteria	Ground	Low Vegetation	Medium Vegetation	High Vegetation	Roofs	Facade	Vehicle
GEO_ONLY	0.57	0.07	0.66	0.02	0.47	0.7	0.01
HEI_ONLY	0.8	0.3	0.68	0.13	0.76	0.61	0.24
COL_ONLY	0.67	0.24	0.87	0.12	0.72	0.73	0.21
GEO_COL	0.83	0.46	0.91	0.08	0.84	0.92	0.49
COL_HEI	0.67	0.24	0.87	0.12	0.72	0.73	0.21
ALL_FEAT	0.95	0.8	0.95	0.63	0.95	0.95	0.84
NO_GROUND	NA	0.86	0.96	0.65	0.96	0.96	0.89

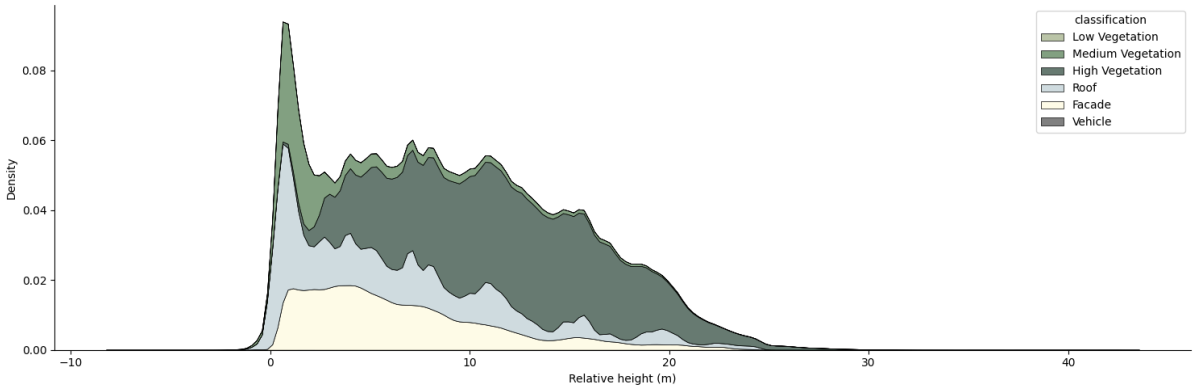

Figure A1. Density distribution of relative height values in the classified point cloud (in meters).

Multi-scale classification of photogrammetric point cloud data: Towards Establishing a Digital Twin in Louvain-la-Neuve

Sinoj Kokulasingam

Under the context of establishing a digital twin, the first step after data collection is to extract meaningful information from dense big data. This work provides a starting point by semantically labelling a photogrammetric point cloud dataset and seeks to find the optimal descriptors for extracting building information in a study area within Louvain-la-Neuve. A multi-scale point-wise classification approach was adopted where the point cloud was iteratively subsampled three times at three progressively larger grid sizes. At each subsample, 15 feature descriptors derived from height, reflectance, and eigenvalue-based geometry were computed using exclusively free and open-source software. The model with all features combined performed the best achieving an overall accuracy of 0.94, though with major confusion between roof and ground points. Although, geometric features performed the worst reaching a low of 0.59 overall accuracy, it was proven that the combination of geometric features with other color or height information led to more accurate classification of roofs and facades. Moreover, the reflectance information from photogrammetry proved to be highly valuable for vegetation extraction. In order to evade the confusion between roof and ground, the ground points were segmented using Cloth Simulation Filter (CSF) followed by the reconstruction of a gapless DEM. This approach showed great potential as since it enhanced the classification accuracy reaching 95% overall accuracy without the introduction of external datasets. However, further validation of roof points with a rooftop dataset from the Wallonian cartographic dataset (PICC) showed that a quarter of points classified as roof were needed to be removed to attain a 91% validation accuracy.

UNIVERSITÉ CATHOLIQUE DE LOUVAIN
Faculté des bioingénieurs
Croix du Sud, 2 bte L7.05.01, 1348 Louvain-la-Neuve, Belgique | **www.uclouvain.be/agro**